

Humboldt-Universität zu Berlin
Mathematisch-Naturwissenschaftliche Fakultät I

Optical and Spin Coherence Properties of Nitrogen Vacancy Centers in Nano Diamond

**Masterarbeit zur Erlangung des akademischen Grades
Master of Science (M.Sc.)
im Fach Physik**

Bernd Sontheimer

13. November 2014

Gutachter:
Prof. Dr. Oliver Benson,
Prof. Dr. Beate Röder

Zusammenfassung

Die vorliegende Arbeit befasst sich mit der experimentellen Untersuchung der Optischen- und Spin-Kohärenzeigenschaften einzelner Stickstofffehlstellenzentren in Nanodiamanten. Hierzu werden zunächst Versuchsabläufe, vom Finden einzelner Stickstofffehlstellenzentren bis hin zur Bestimmung ihrer charakteristischen Spin-Kohärenzzeiten T_2^* und T_2 mit Hilfe von kohärenten Spinmanipulationsexperimenten, entwickelt und teilweise automatisiert. Dies ermöglicht die effiziente statistische Untersuchung vieler Stickstofffehlstellenzentren in verschiedenen Arten von Nanodiamanten. Danach wird die optische Kohärenz der Nullphononenlinie bei kryogenen Temperaturen in einem Zweiphotoneninterferenzexperiment untersucht.

Abstract

In this thesis, the optical and spin coherence properties of single nitrogen vacancy centers in nano diamond are experimentally investigated. Therefore, measurement protocols, that begin with finding single nitrogen vacancy centers in nano diamonds and end with performing coherent spin manipulation experiments on them to reveal their characteristic spin coherence times T_2^* and T_2 , are developed and partially automated. This enables efficient statistical measurements of many nitrogen vacancy centers in different types of nano diamond. Then, the optical coherence of the zero phonon line is investigated in a two photon interference experiment.

Contents

1	Introduction	7
2	Theory	8
2.1	Light-matter interaction	8
2.1.1	Photon detection	8
2.1.2	Hong-Ou-Mandel effect	10
2.1.3	Rate equations of the three level system	11
2.1.4	Saturation behavior of the three level system	14
2.1.5	Optical Bloch equations	16
2.1.6	Rabi oscillations	19
2.2	Nitrogen vacancy centers in diamond	21
2.2.1	Optical properties	22
2.2.2	Spin properties	23
2.2.3	Nano diamonds	24
3	Experimentals	25
3.1	Spin coherence of the NV center	25
3.1.1	Setup	25
3.1.2	Sample and Preparation	28
3.1.3	Methods	29
3.1.4	Results	33
3.2	Two photon quantum interference with a single NV center	39
3.2.1	Setup	39
3.2.2	Sample and Preparation	42
3.2.3	Methods	43
3.2.4	Results	44
4	Conclusion and outlook	47

1 Introduction

Technology and science have always been driven by the desire to make devices and functional structures smaller, more powerful and thus more efficient. A parade example for this are microprocessors in today's computers. Since Intel launched its first microprocessor with a structure width of 10 µm in 1971, the miniaturization progressed exponentially over time and is currently at a 22 nm process, already reaching and surpassing the limits of classical physics.[1]

To improve the efficiency of such systems even further makes the understanding of quantum processes and the application of quantum phenomena indispensable. Complementary to conventional computers, it has been proven theoretically that certain mathematical problems, i.e. the factorization of integers, can be solved much more efficiently with quantum algorithms and quantum computers.[2] Today, a physical implementation of a quantum computer is still in the need of a system that can be used as quantum bits (qubits). In contrast to the classical bit which can either be "1" or "0", the qubit is a superposition of both of these states. In the past, several systems, such as electrons in quantum dots or trapped ions, were already employed as single qubits, but a tremendous technical effort, i.e. cooling to cryogenic temperatures, was needed to reveal their quantum behavior.[3] The nitrogen vacancy center in diamond is a very promising candidate for a relatively easy to handle qubit.[4, 5] Whilst being embedded in a stable solid state system, it mirrors the behavior of a trapped ion, having a strong optical transition and an addressable electron spin with measured coherence times up to the millisecond regime in bulk diamond.[6]

In the past decades, research on nitrogen vacancy centers has advanced tremendously. First optically detected magnetic resonance measurements on single nitrogen vacancy centers in diamond were performed in 1997 by Gruber et. al. [7] Since then, many experiments employed the NV center's observable quantum behavior to perform basic non-classical experiments like the quantum Zeno effect or even the entanglement of two electron spins in spatially separated nitrogen vacancy centers.[8, 9] Furthermore, applications were developed that use NV centers embedded in nano diamonds as magnetic field probes for mapping the local density of photonic states and fluorescent markers in biology.[10, 11, 12, 13]

The motivation for this work is to develop methods to measure and understand the mechanics that influence the nitrogen vacancy centers in nano diamonds in order to improve their performance for future applications. Therefore, systematical studies of the optical and spin coherence properties of NV centers in different types nano diamonds are performed.

2 Theory

This chapter covers the fundamental theory required for the experiments performed in Chapter 3. First, relevant aspects of light-matter interaction are introduced. In this context, the theory of photon detection and its statistics for single photon sources are presented. The Hong-Ou-Mandel effect, a quantum mechanical two photon interference phenomenon and the dynamics of a three level system which will resemble the one of the later investigated nitrogen vacancy center (NV center) are discussed. Later, principles of coherent interactions between an external field and a two level system are derived in the form of optical Bloch equations and the resulting Rabi oscillation.

In Section 2.2 the nitrogen vacancy center (NV center) with its unique optical and spin properties is examined. A simplified energy level scheme is used to explain these properties. The chapter closes with a discussion on the effects that occur if the dimensions of the diamond that hosts the NV center are scaled down to the order of nanometers.

2.1 Light-matter interaction

2.1.1 Photon detection

A crucial part of the experiments discussed in this thesis is the detection of single photons. Usually, detection is achieved by absorbing a photon and thereby transferring its energy to the detector material where a measurable macroscopic effect is triggered. For instance, in avalanche photo diodes (APDs), this energy raises an electron from the valence band to the conduction band (inner photoelectric effect) of a semi conductor diode generating a electron-hole pair. The now free charge carrier is accelerated by a strong electrical field gradient and generates more electron-hole pairs via collisions with bound electrons. This avalanche effect results in a detectable macroscopic current.

With an initial photon state $|\phi\rangle$, the probability to detect one photon N_{det} is proportional to the average number of photons available, which is the expectation value of the number operator \hat{n} . Therefore it can be expressed as

$$N_{det} = \eta \langle \hat{n} \rangle = \eta \langle \phi | \hat{a}^\dagger \hat{a} | \phi \rangle, \quad (2.1)$$

with the quantum mechanical creation and annihilation operators \hat{a}^\dagger and \hat{a} and the detection efficiency η .[8]

After detecting the photon, the new wave function $|\phi'\rangle$ contains one photon less and thus can be created by acting with the annihilation operator $\hat{a}(t)$ on the initial state at a time t . After renormalization this results in

$$|\phi'\rangle = \frac{\hat{a}(t)}{\sqrt{\langle \hat{n}(t) \rangle}} |\phi\rangle. \quad (2.2)$$

Inserting this into Equation 2.1, the probability to detect a second photon at time $t + \tau$ after the detection of a photon at time t becomes

$$\begin{aligned} N(t, t + \tau) &= \eta \langle \phi' | \hat{a}^\dagger(t + \tau) \hat{a}(t + \tau) | \phi' \rangle \\ &= \frac{\eta}{\langle \hat{n}(t) \rangle} \langle \phi | \hat{a}^\dagger(t) \hat{a}^\dagger(t + \tau) \hat{a}(t + \tau) \hat{a}(t) | \phi \rangle. \end{aligned} \quad (2.3)$$

Multiplication with the photon detection probability at time t results in the second order correlation function [14]

$$G^{(2)}(t, t + \tau) = \eta^2 \langle \phi | \hat{a}^\dagger(t) \hat{a}^\dagger(t + \tau) \hat{a}(t + \tau) \hat{a}(t) | \phi \rangle. \quad (2.4)$$

Usually this function is given in a normalized form where the quantum efficiency is omitted and the time t of the first detected photon is set to zero. Therefore, it is commonly found as

$$g^{(2)}(\tau) = \frac{\langle \phi | \hat{a}^\dagger(0) \hat{a}^\dagger(\tau) \hat{a}(\tau) \hat{a}(0) | \phi \rangle}{\langle \phi | \hat{a}^\dagger(0) \hat{a}(0) | \phi \rangle \langle \phi | \hat{a}^\dagger(\tau) \hat{a}(\tau) | \phi \rangle}. \quad (2.5)$$

The behavior of this function at zero time delay can be used to distinguish between light sources. At $\tau = 0$ Equation 2.5 becomes

$$g^{(2)}(0) = \frac{\langle \phi | \hat{a}^\dagger \hat{a}^\dagger \hat{a} \hat{a} | \phi \rangle}{\langle \phi | \hat{a}^\dagger \hat{a} | \phi \rangle^2}. \quad (2.6)$$

Laser light, for instance, can be described by coherent states, which are eigenstates of the annihilation operator ($\hat{a} |\phi\rangle = \alpha |\phi\rangle$). The second order correlation function then simply yields

$$g^{(2)}(0) = 1. \quad (2.7)$$

In contrast, light of a single photon emitter can be represented as a Fock state, which is an eigenstate of the number operator ($n |\phi\rangle = \hat{n} |\phi\rangle$). Using the commutation relation $[\hat{a}, \hat{a}^\dagger] = 1$, the following relation for $\tau = 0$ can be derived:

$$\begin{aligned} g^{(2)}(0) &= \frac{\langle \phi | \hat{a}^\dagger (\hat{a} \hat{a}^\dagger - 1) \hat{a} | \phi \rangle}{\langle \phi | \hat{a}^\dagger \hat{a} | \phi \rangle^2} \\ &= \frac{\langle \phi | \hat{n} \hat{n} | \phi \rangle - \langle \phi | \hat{n} | \phi \rangle}{\langle \phi | \hat{n} | \phi \rangle^2} \\ &= 1 - \frac{1}{n}. \end{aligned} \quad (2.8)$$

For small initial photon numbers $n = 0, 1$ (zero or single photon emitter), the second order correlation function vanishes whereas in the limit of $n \rightarrow \infty$ it reaches towards the result of the coherent state $g^{(2)}(0) = 1$. Therefore, in an experiment, a recorded value of $g^{(2)}(0) \leq 0.5$ is a strong indicator that the observed light is predominantly emitted by one single photon emitter.

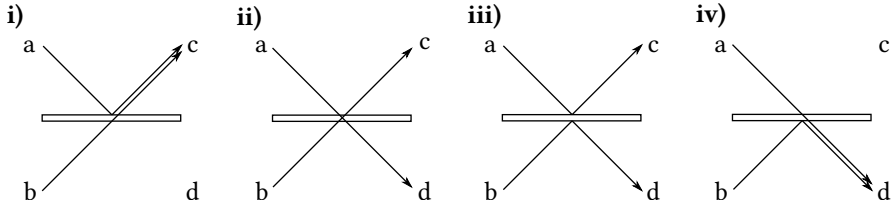


Figure 2.1: Illustration of the Hong-Ou-Mandel effect. Classically one would expect all four possibilities as an outcome of the experiment. Quantummechanically, if the two incident photons are indistinguishable, **ii)** and **iii)** cancel each other and only the cases **i)** and **iv)** occur.

2.1.2 Hong-Ou-Mandel effect

If two identical photons in different spacial modes a and b with corresponding creation operators \hat{a}^\dagger and \hat{b}^\dagger enter a 50:50 beam splitter one on each input port, they will always bunch together and exit the beam splitter in the same but random output port. This effect was demonstrated in 1987 by the three physicists C. K. Hong, Z. Y. Ou and Leonard Mandel and is therefore named after them.[15] Figure 2.1 shows a scheme of the effect. Mathematically, a beam splitter can be represented by a unitary transformation U_{BS} which transforms the creation operators as follows:

$$\begin{pmatrix} \hat{a}^\dagger \\ \hat{b}^\dagger \end{pmatrix} \xrightarrow{U_{BS}} \frac{1}{\sqrt{2}} \begin{pmatrix} 1 & 1 \\ 1 & -1 \end{pmatrix} \begin{pmatrix} \hat{c}^\dagger \\ \hat{d}^\dagger \end{pmatrix}. \quad (2.9)$$

Physically, this means the reflection at one surface of the beam splitter induces a relative phase shift of -1 with respect to reflection at the other side of the beam splitter. When two photons enter the beam splitter, the state of the modes becomes

$$\begin{aligned} |1,1\rangle_{ab} &= \hat{a}^\dagger \hat{b}^\dagger |0,0\rangle_{ab} \xrightarrow{U_{BS}} \frac{1}{2} (\hat{c}^\dagger + \hat{d}^\dagger)(\hat{c}^\dagger - \hat{d}^\dagger) |0,0\rangle_{cd} \\ &= \frac{1}{2} (\hat{c}^{\dagger 2} - \hat{d}^{\dagger 2}) |0,0\rangle_{cd} \\ &= \frac{1}{\sqrt{2}} (|2,0\rangle_{cd} - |0,2\rangle_{cd}). \end{aligned} \quad (2.10)$$

Here, the fact that the commutator of the two creation operators \hat{c}^\dagger and \hat{d}^\dagger vanishes was used. The two photons are either created both in the c or both in the d mode. The resulting two photon state is maximally entangled and the simplest non-trivial state in the class called *NOON* states.[16]

In experiments, the Hong-Ou-Mandel effect is often measured by connecting each output port of the beam splitter to an avalanche photo diode and record the coincidence counts between incoming identical photons for different relative time delays $\delta\tau$ between the photons. In the initial experiment, Hong, Ou and Mandel used photon pairs produced from a parametric downconversion source and controlled the delay by shifting

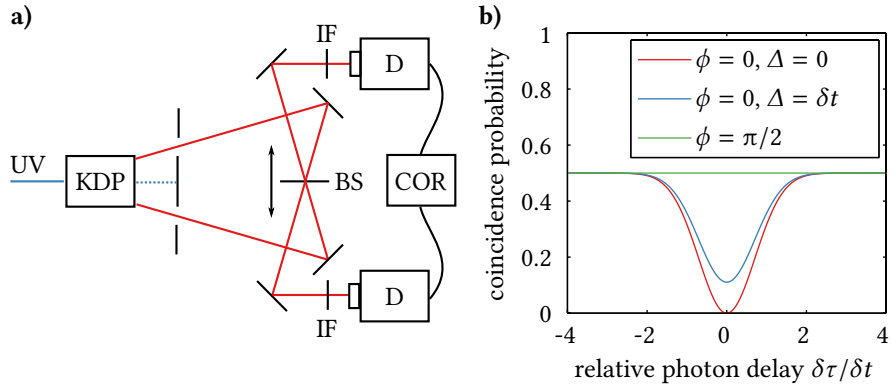


Figure 2.2: **a)** Simplified schematics of the original Hong-Ou-Mandel setup adapted from Hong et. al.[15] Two photons are created via parametric downconversion of UV light in a potassium dihydrogen phosphate crystal (KDP). The interference filters (IF) determine the uncertainties of the generated photon frequencies. By moving the beam splitter (BS) the photon arrival times $\delta\tau$ at the beam splitter are varied. **b)** Results of Equation 2.11 for different phase relations ϕ frequency differences Δ .

the position of the beam splitter.[15] For two impinging linear polarized photons the coincidence probability $P^{(2)}$ dependent on photon the delay $\delta\tau$, the angle between the photon polarizations φ and the frequency difference Δ of the photons is given by

$$P^{(2)} = \frac{1}{2} \left(1 - \cos^2 \varphi \exp \left(-\frac{\delta t^2}{4/\Delta^2} \right) \exp \left(-\frac{\delta\tau^2}{\delta t^2} \right) \right), \quad (2.11)$$

where δt is the length of the Gaussian-shaped photons and perfect detection efficiency of the photons is assumed.[17]

Figure 2.2 shows the coincidence probability as a function of the photon delay $\delta\tau$ for different photon polarizations and frequency differences. Perpendicular polarized photon pairs $\varphi = \pi/2$ show no interference at all. For them, the probability to detect the photons at different ports of the beam splitter is always 1/2. In conclusion, photon pairs with identical polarization $\varphi = 0$ show a Gaussian shaped Hong-Ou-Mandel dip with the width δt centered at $\delta\tau = 0$ and a maximum dip depth for identical frequencies $\Delta = 0$. As a result, two-photon interference can be used to test the indistinguishability of photons.

2.1.3 Rate equations of the three level system

As a preparation for the energy level scheme of the nitrogen vacancy center discussed in Section 2.2, a simple three level system consisting of ground state $|g\rangle$, an excited state $|e\rangle$ and an additional shelving state $|s\rangle$ is discussed here. The dynamics of such a single system is investigated adapting approaches from [18], [19] and [8]. It is assumed that radiative emission occurs spontaneously and solely by relaxing from the excited state to

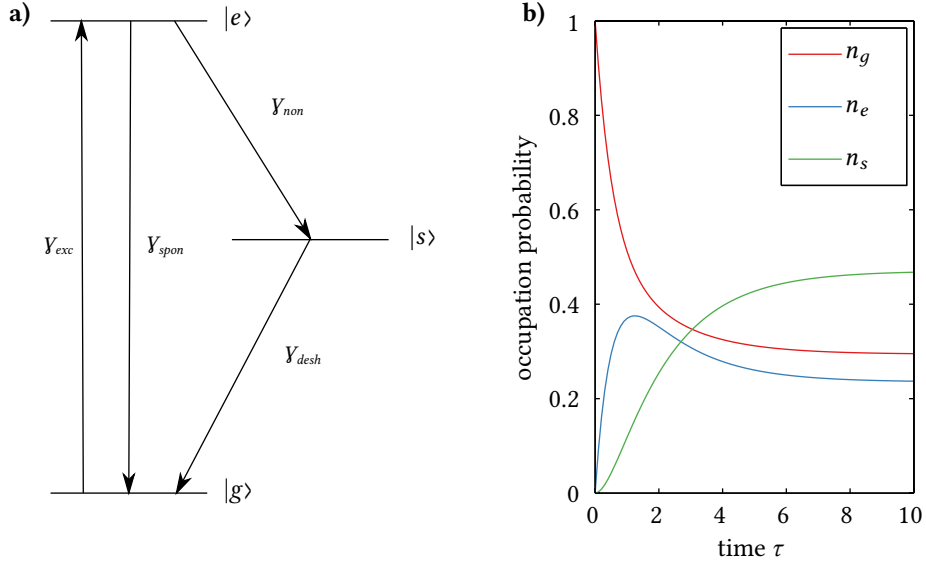


Figure 2.3: a) Energy scheme of a simple three level system consisting of ground state $|g\rangle$, excited state $|e\rangle$ and shelving state $|s\rangle$ and the corresponding transmission coefficients γ_i . b) Dynamics of the occupation probabilities for the different states calculated after the emission of one photon with $\gamma_{exc} = 1$, $\gamma_{spon} = 0.75$, $\gamma_{non} = 0.5$ and $\gamma_{desh} = 0.25$.

the ground state. Transitions to and from an additional shelving state are regarded as non radiative. The transition rates are labeled γ_i and the occupation probabilities of the states n_i .

In such a system, the lifetime of the excited state can be defined as

$$\tau_e = \frac{1}{\gamma_{spon} + \gamma_{non}} \quad (2.12)$$

and the full dynamics are described by the following set of differential equations:

$$\begin{aligned} \frac{d}{dt} n_g(t) &= -\gamma_{exc} n_g(t) + \gamma_{spon} n_e(t) + \gamma_{desh} n_s(t) \\ \frac{d}{dt} n_e(t) &= \gamma_{exc} n_g(t) - \gamma_{spon} n_e(t) - \gamma_{non} n_e(t) \\ \frac{d}{dt} n_s(t) &= \gamma_{non} n_e(t) - \gamma_{desh} n_s(t) \end{aligned} \quad (2.13)$$

This homogenous linear system of differential equations can also be written in matrix form which can be diagonalized to find the eigenvalues

$$\begin{aligned} \lambda_1 &= 0 \\ \lambda_{2,3} &= \frac{-S \pm \sqrt{S^2 - 4T}}{2}, \end{aligned} \quad (2.14)$$

with

$$\begin{aligned} S &= \gamma_{exc} + \gamma_{spon} + \gamma_{non} + \gamma_{desh} \\ T &= \gamma_{exc}\gamma_{desh} + \gamma_{exc}\gamma_{non} + \gamma_{desh}\gamma_{non} + \gamma_{desh}\gamma_{spon}. \end{aligned} \quad (2.15)$$

With those eigenvalues, the corresponding eigenvectors and straight line solutions can be calculated. Finally, the general analytical solution of this system of differential equations is the sum of the linear independent straight line solutions. This expression is quite lengthy which is why in the following only results of relevant parts will be shown. As discussed in Section 2.1.1, the $g^{(2)}$ function describes the probability to detect a second photon after a time delay τ after a (start) photon at $t = 0$ is detected. In the experiment, only light spontaneously emitted for transitions from the excited state to the ground state is observed. This means that after detecting a photon the system is always in the ground state with $n_g(0) = 1$, $n_e(0) = 0$, $n_s(0) = 0$. The solutions of Equation 2.13 resulting from these initial conditions are illustrated in Figure 2.3 for the arbitrarily chosen coefficients $\gamma_{exc} = 1$, $\gamma_{spon} = 0.75$, $\gamma_{non} = 0.5$ and $\gamma_{desh} = 0.25$.

The probability to detect a second photon after a time τ is directly proportional to the solution of the occupation probability of the excited state $n_e(t)$ multiplied by the emission coefficient γ_{spon} . By taking into account the quantum efficiency η introduced in Equation 2.1, the unnormalized $G^{(2)}$ function is given by

$$G^{(2)}(\tau) = \eta\gamma_{spon}n_e(\tau). \quad (2.16)$$

For better comparability, this will be normalized with the limit of the $G^{(2)}(\tau)$ at large times $\tau \rightarrow \infty$. At this limit, the dynamics of the Equations 2.13 come to rest and therefore $n_e(\infty)$ can be obtained by calculating their steady state solutions. This is accomplished by setting the derivatives on the left hand side to zero, thereby losing the time dependency of the average occupation probabilities. Additionally, the sum of the probabilities $n_g + n_e + n_s$ must be one, because the system has to be in either one of the states. Solving the resulting system of equations for n_e results in

$$n_e(\infty) = \frac{\gamma_{desh}\gamma_{exc}}{T}. \quad (2.17)$$

The normalized $g^{(2)}$ function then becomes

$$g^{(2)}(\tau) = 1 - (1 + A)e^{\lambda_2\tau} + Ae^{\lambda_3\tau}, \quad (2.18)$$

with

$$A = \frac{\lambda_3 + \gamma_{desh} - \gamma_{exc}\frac{\gamma_{non}}{\gamma_{desh}}}{\lambda_2 + \lambda_3}. \quad (2.19)$$

As expected, the $g^{(2)}$ function vanishes for zero time delay, since the system under study only emits one photon at a time. The behavior when $g^{(2)} < 1$ is called antibunching. For certain coefficients γ_i , at small time delays τ the $g^{(2)}$ function reaches values higher than one. This is called bunching. As shown in Figure 2.4, the height and the width of

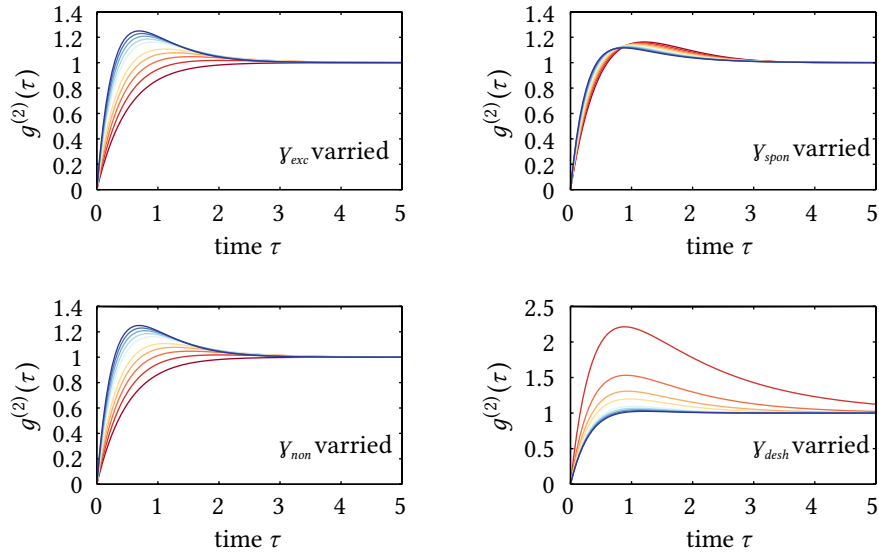


Figure 2.4: Second order correlation function for different values of the coefficients γ_i . The graphs show the behavior of the $g^{(2)}$ function if three of the coefficients are set to one and the remaining one is changed in 0.2 increments from zero (red) to two (blue).

this feature are determined by a combination of all four transition rates and can not be attributed to a single parameter. The reason for this bunching effect is the shelving state. After the first photon is detected, the system is not trapped in the shelving state and spontaneous emission of a second photon is more likely than in average.

2.1.4 Saturation behavior of the three level system

From the steady state occupation probability for $n_e(\infty)$ calculated in Equation 2.17 information about the maximal emission rate of the system under continuous excitation, for example by a cw laser, can be derived. The emission rate R can be defined as

$$R = \gamma_{spon} n_e(\infty). \quad (2.20)$$

After inserting Equation 2.17 and Equation 2.15, this becomes

$$R = \frac{\gamma_{spon} \gamma_{desh} \gamma_{exc}}{\gamma_{exc} \gamma_{desh} + \gamma_{exc} \gamma_{non} + \gamma_{desh} \gamma_{non} + \gamma_{desh} \gamma_{spon}}. \quad (2.21)$$

Generally it is rather tedious or sometimes even impossible to determine all the transition coefficients γ_i in an experiment. But to assume a linear dependency between an incoming laser intensity and the excitation rate $I = \alpha_I \gamma_{exc}$ seems pellucid. The rate

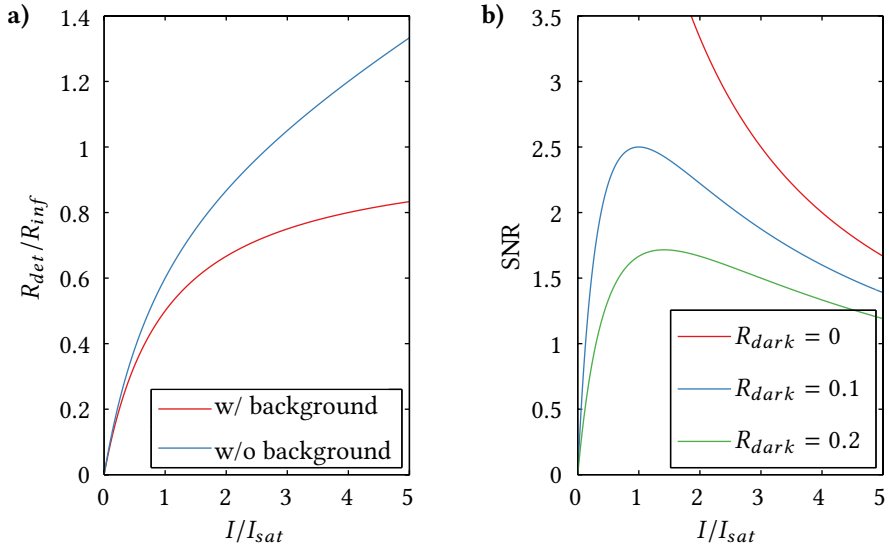


Figure 2.5: Saturation behavior of the three level system. **a)** Influence of the background emission on the photon detection rate ($\alpha_{bg} = 0.1$, $N_{dark} = 0$). **b)** Influence of the dark count rate on the signal to noise ratio (SNR) at $\alpha_{bg} = 0.1$.

R_{inf} at infinite excitation intensity and the saturation intensity I_{sat} where $R = R_{inf}/2$ are then straight forward calculated to be

$$R_{inf} = \frac{\gamma_{desh}\gamma_{spont}}{\gamma_{desh} + \gamma_{non}}, \quad (2.22)$$

$$I_{sat} = \alpha_I \frac{\gamma_{desh}(\gamma_{non} + \gamma_{spont})}{\gamma_{desh} + \gamma_{non}}.$$

With this, R can be expressed as

$$R(I) = \frac{R_{inf}I}{I_{sat} + I}. \quad (2.23)$$

Notably, in the final result the constant α_I cancels out.

In an experiment, the rate R is measured by counting the emitted photons with a detector, i. e. an APD, that has a certain intrinsic dark count rate R_{dark} . Furthermore, the observed system is usually embedded in an environment that will also be excited by the laser and therefore generates background photons linearly dependent on the excitation intensity. The adapted Equation 2.23 which takes this into consideration reads

$$R_{det}(I) = \frac{R_{inf}I}{I_{sat} + I} + \alpha_{bg}I + R_{dark}. \quad (2.24)$$

Figure 2.5 illustrates the obtained results. It becomes evident that only in the low excitation regime the detected count rate increases linearly with the intensity. This behavior is typical for quantum emitters [8].

The signal to noise ratio can be defined as the ratio between the emission rate R and the sum of dark count rate R_{dark} and the rate due to the background $\alpha_{bg}I$. As seen in Figure 2.5, the decreasing signal to noise ratio for high excitation intensities limits the intensity reasonably used in the experiment.

2.1.5 Optical Bloch equations

In this section, the dynamics of a two level system exposed to a strong external field of frequency ω are investigated following approaches from [20] and [21]. In contrast to the section before, this will not be achieved in a classical framework, but quantumechanical operators and quantities like coherences will be introduced. The Hamiltonian of such a system can be decomposed to a stationary Hamiltonian $\hat{\mathcal{H}}_E$, an interaction Hamiltonian $\hat{\mathcal{H}}_I$ and a Hamiltonian $\hat{\mathcal{H}}_R$ which accounts for relaxation processes:

$$\hat{\mathcal{H}} = \hat{\mathcal{H}}_E + \hat{\mathcal{H}}_I + \hat{\mathcal{H}}_R. \quad (2.25)$$

The system consisting of a ground state $|g\rangle$ and excited state $|e\rangle$ can be written by the wave function $|\psi\rangle = c_g|g\rangle + c_e|e\rangle$ with c_e and c_g being complex numbers fulfilling $|c_g|^2 + |c_e|^2 = 1$ and $|g\rangle$ and $|e\rangle$ being the eigenstate basis

$$|g\rangle = \begin{pmatrix} 1 \\ 0 \end{pmatrix}, |e\rangle = \begin{pmatrix} 0 \\ 1 \end{pmatrix}. \quad (2.26)$$

The matrix elements ρ_{ij} of the density matrix $\hat{\rho} = |\psi\rangle\langle\psi|$ then write as

$$\begin{aligned} \rho_{gg} &= c_g c_g^* \\ \rho_{ee} &= c_e c_e^* \\ \rho_{ge} &= c_g c_e^* = \rho_{eg}^*. \end{aligned} \quad (2.27)$$

The digonal elements ρ_{ii} of the density matrix are termed populations and the off-diagonal elements ρ_{ij} are known as coherences. Finally, the time evolution of the density matrix is given by the von Neuman equation

$$i\hbar \frac{d}{dt} \hat{\rho} = [\hat{\mathcal{H}}, \hat{\rho}]. \quad (2.28)$$

In the next passages, the individual terms of the decomposed Hamiltonian will be investigated in order to solve the dynamics of the whole system.

For the stationary Hamiltonian which corresponds to the system without any external field and relaxation processes the time independent Schrödinger equation $\hat{\mathcal{H}}|\psi\rangle = \hat{E}|\psi\rangle$ directly gives

$$\hat{\mathcal{H}}_E = i\hbar\partial_t = \begin{pmatrix} E_g & 0 \\ 0 & E_e \end{pmatrix} \quad (2.29)$$

in the eigenstate basis with the energy eigenvalues E_g and E_e of the ground and the excited state.

Next, with an apparent oscillating field $\mathbf{E}(t) = \mathbf{E}_0 \cos \omega t$, the interaction Hamiltonian $\hat{\mathcal{H}}_I = -\hat{\mathbf{D}} \cdot \mathbf{E}(t)$ in the dipole approximation becomes

$$\hat{\mathcal{H}}_I = -\hat{\mathbf{D}} \cdot \mathbf{E}_0 \cos \omega t. \quad (2.30)$$

Considering parity, the dipole term between equal states vanishes $\langle g | \hat{\mathbf{D}} | g \rangle = \langle e | \hat{\mathbf{D}} | e \rangle = 0$, leaving only the dipole matrix elements $\mathbf{d} = \langle g | \hat{\mathbf{D}} | e \rangle = \langle g | \hat{\mathbf{D}} | e \rangle$. Therefore, the Hamiltonian can be rewritten in matrix formalism as

$$\begin{aligned} \hat{\mathcal{H}} &= \begin{pmatrix} 0 & -\hbar\Omega \cos \omega t \\ -\hbar\Omega \cos \omega t & 0 \end{pmatrix}, \\ &= \begin{pmatrix} 0 & -\frac{\hbar\Omega}{2}(e^{i\omega t} + e^{-i\omega t}) \\ -\frac{\hbar\Omega}{2}(e^{i\omega t} + e^{-i\omega t}) & 0 \end{pmatrix}. \end{aligned} \quad (2.31)$$

where the Rabi frequency $\Omega = (\mathbf{d} \cdot \mathbf{E}_0)/\hbar$ was introduced.

The relaxation component of the decomposed Hamiltonian will be introduced in a phenomenological way, using similar ideas that lead to the rate equations in Section 2.1.3. From an experimental point of view, it is feasible to include a decay rate Γ which leads to a lifetime $T_e = 1/\Gamma$. If no energy is added to the system, the ground state is considered to be stable, and therefore its lifetime T_g goes to infinity. Also, it is evident that population changes in the excited state can only end up refilling the ground state. With Equation 2.28, these thoughts can be expressed as

$$\begin{aligned} (i\hbar)^{-1} [\hat{\mathcal{H}}_R, \hat{\rho}]_{ee} &= -\frac{1}{T_e} \rho_{ee} = -\Gamma \rho_{ee}, \\ (i\hbar)^{-1} [\hat{\mathcal{H}}_R, \hat{\rho}]_{gg} &= +\frac{1}{T_e} \rho_{ee} = +\Gamma \rho_{ee}. \end{aligned} \quad (2.32)$$

Here, the indices at the commutator specify the matrix element of the resulting Hamiltonian that is investigated. The off-diagonal coherences are assumed to decay both with an equal rate $\gamma = 1/T_c$ due to e.g. random fluctuations of the field intensities on a short time scale or collisions with the environment. Their dynamics can be expressed as

$$\begin{aligned} (i\hbar)^{-1} [\hat{\mathcal{H}}_R, \hat{\rho}]_{ge} &= -\frac{1}{T_c} \rho_{ge} = -\gamma \rho_{ge}, \\ (i\hbar)^{-1} [\hat{\mathcal{H}}_R, \hat{\rho}]_{eg} &= -\frac{1}{T_c} \rho_{eg} = -\gamma \rho_{eg}. \end{aligned} \quad (2.33)$$

The coherence lifetime T_c corresponds to the lifetimes of the excited and ground states as follows from [21]:

$$\frac{1}{T_c} = \frac{1}{2} \left(\frac{1}{T_g} + \frac{1}{T_e} \right) \quad (2.34)$$

Therefore, the equations $T_c = 2T_e$ and $2\gamma = \Gamma$ hold, since only decay from the excited to the ground state is considered ($T_g = \infty$). In the real world, static local field inhomogeneities perturb the phase relation between the exciting field and the coherently driven

system. This dephasing can be taken into account by adding a dephasing rate $\gamma_\phi = 1/T_\phi$ to the decoherence rate $\gamma = 1/T_c$, resulting into an altered decoherence time

$$\frac{1}{T_c^*} = \frac{1}{T_c} + \frac{1}{T_\phi}. \quad (2.35)$$

Additionally, dephasing effects can therefore be considered by simply replacing T_c with T_c^* or respectively γ with γ^* in the following equations.

As a remark, in common literature, the naming of the lifetimes is often different. The lifetime $T_e = 1/\Gamma$ of the excited state is often called longitudinal relaxation time and is termed T_1 time, while the lifetime $T_c = 1/\gamma$ is known as transverse relaxation time or T_2 time. Consequently, the T_c^* time is referred to as T_2^* time. Furthermore, in most real world experiments the relation $T_1 \gg T_2 > T_2^*$ holds.

In summary, the dynamics of Hamiltonian $\hat{\mathcal{H}}_R$ become

$$[\hat{\mathcal{H}}_R, \hat{\rho}] = i\hbar \begin{pmatrix} \Gamma\rho_{ee} & -\gamma\rho_{ge} \\ -\gamma\rho_{eg} & -\Gamma\rho_{ee} \end{pmatrix}, \quad (2.36)$$

Inserting Equation 2.27, Equation 2.29 and Equation 2.31 into the von Neumann equation and adding the phenomenological introduced Equation 2.36, the complete dynamics of the two levels system interacting with the radiation field yields

$$\begin{aligned} i\hbar \frac{d}{dt} \rho_{gg} &= \frac{i\Omega}{2} (\rho_{eg} - \rho_{ge}) (e^{i\omega t} + e^{-i\omega t}) + i\hbar\Gamma\rho_{ee} \\ i\hbar \frac{d}{dt} \rho_{ge} &= \frac{i\Omega}{2} (\rho_{ee} - \rho_{gg}) (e^{i\omega t} + e^{-i\omega t}) + \rho_{ge} (E_1 - E_2) - i\hbar\gamma\rho_{ge} \\ i\hbar \frac{d}{dt} \rho_{eg} &= \frac{i\Omega}{2} (\rho_{gg} - \rho_{ee}) (e^{i\omega t} + e^{-i\omega t}) + \rho_{eg} (E_2 - E_1) - i\hbar\gamma\rho_{eg} \\ i\hbar \frac{d}{dt} \rho_{ee} &= \frac{i\Omega}{2} (\rho_{ge} - \rho_{eg}) (e^{i\omega t} + e^{-i\omega t}) - i\hbar\Gamma\rho_{ee} \end{aligned} \quad (2.37)$$

This can be further simplified by converting the energy differences into frequencies $\omega_{ij} = (E_i - E_j)/\hbar$ and introducing the detuning $\Delta = \omega_{eg} - \omega$ as well as transferring to a rotating frame with

$$\begin{aligned} \rho_{ge} &= \rho'_{ge} e^{i\omega t} \\ \rho_{eg} &= \rho'_{eg} e^{-i\omega t}. \end{aligned} \quad (2.38)$$

Now, after omitting fast oscillating terms with a frequency of 2ω (rotating wave approximation), the final result reads:

$$\begin{aligned} \frac{d}{dt} \rho_{gg} &= \frac{i\Omega}{2} (\rho'_{eg} - \rho'_{ge}) + \Gamma\rho_{ee} \\ \frac{d}{dt} \rho'_{ge} &= \frac{i\Omega}{2} (\rho_{ee} - \rho_{gg}) + (\gamma + i\Delta)\rho'_{ge} \\ \frac{d}{dt} \rho'_{eg} &= \frac{i\Omega}{2} (\rho_{gg} - \rho_{ee}) + (\gamma - i\Delta)\rho'_{eg} \\ \frac{d}{dt} \rho_{ee} &= \frac{i\Omega}{2} (\rho'_{ge} - \rho'_{eg}) - \Gamma\rho_{ee} \end{aligned} \quad (2.39)$$

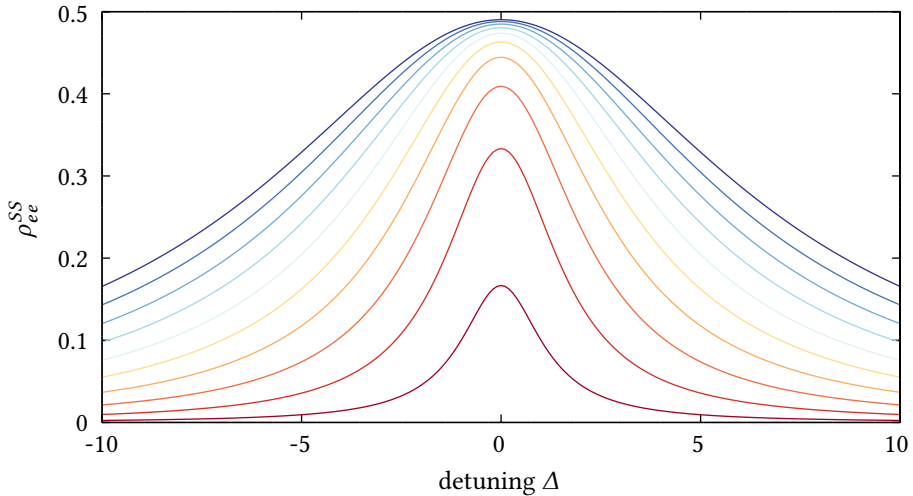


Figure 2.6: Steady state solution of the excited state population ρ_{ee}^{SS} for $\gamma = 1$ and $\Gamma = 2\gamma$ and different Rabi frequencies from $\Omega = 1$ (red line) to $\Omega = 10$ (blue line) in steps of 1Ω .

These equations are known as the optical Bloch equations (OBE). They are similar to the equations derived by Bloch to describe the motion of a spin in a magnetic oscillatory field, since the quantum mechanics of both systems is formally identical.[22]

In some of the experiments performed in Section 3.1, the excited state population is measured as a steady state value. The steady state solutions can be acquired by setting the left hand side of the optical Bloch equations to zero and solving for ρ_{ee} . This yields

$$\rho_{ee}^{SS} = \frac{\gamma\Omega^2}{2(\Gamma\Delta^2 + \gamma^2\Gamma + \gamma\Omega^2)}. \quad (2.40)$$

If only radiation damping is considered ($\gamma = 1/2\Gamma$), this can be further simplified to

$$\rho_{ee}^{SS} = \frac{\Omega^2}{4\Delta^2 + \Gamma^2 + 2\Omega^2}. \quad (2.41)$$

It becomes evident that the steady state solution in dependence of the detuning resambles the shape of a Lorentzian function. The Ω^2 term in the denominator causes a broadening of the width of this function. This effect is illustrated in Figure 2.6 and is commonly referred to as power broadening. Figure 2.6 also shows that the height of the Lorentz peak is dependent on the Rabi frequency and thereby on the intensity of the applied external field. For high intensities, the excited state population converges to 1/2.

2.1.6 Rabi oscillations

Since it is not possible to give general solutions for the optical Bloch Equations 2.39, the two cases of no damping and damping but no detuning will be discussed here.

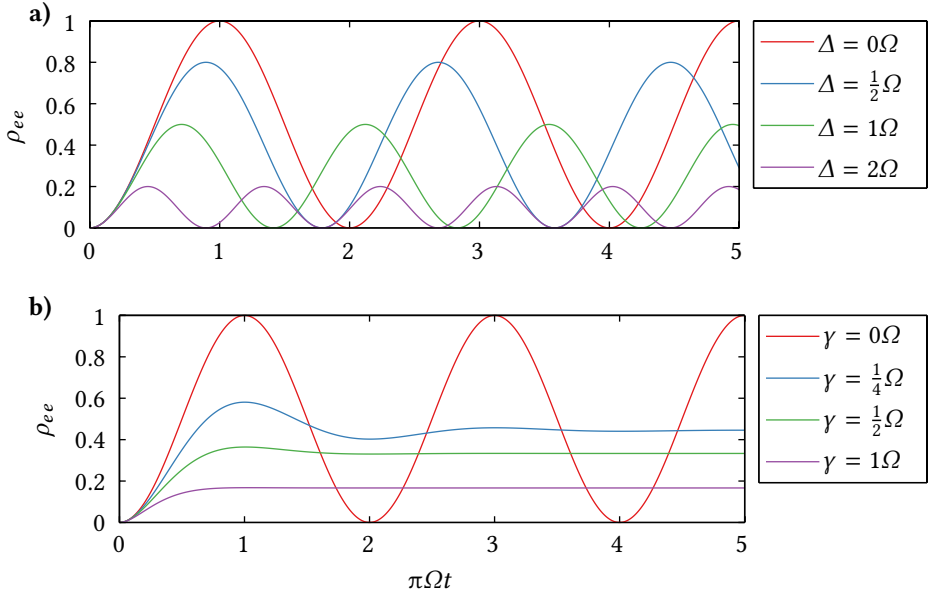


Figure 2.7: Time dependence of the density matrix element ρ_{ee} for **a)** the different values of detuning in the case of no damping, **b)** resonant excitation and different values of damping.

Without damping, $\gamma = \Gamma = 0$ the dynamic of the population of the excited state with the initial conditions $\rho_{ee}(0) = 0$ and $\rho_{ge}(0) = 0$ becomes:

$$\rho_{ee} = \frac{\Omega'^2}{\Omega'^2} \sin^2 \left(\frac{\Omega'}{2} t \right), \quad (2.42)$$

where the generalized Rabi frequency $\Omega' = \sqrt{\Omega^2 + \Delta^2}$ was introduced.[21] The result is illustrated in Figure 2.7 for different values of detuning. The populations are converted in coherences and vice versa and the system thereby oscillates between full population of the ground and the excited state. These oscillations are commonly referred to as Rabi oscillations. By applying the external field for the time $t = \pi/\Omega'$, the population is exactly inverted. Such a pulse is called π -pulse. In the case of resonant excitation, Equation 2.42 simply becomes $\rho_{ee} = \sin^2(\frac{1}{2}\Omega t)$. For higher values of detuning the frequency gets faster while the amplitude decreases.

If damping and dephasing are considered but the detuning is set to zero, the analytical solution for the excited state with the same initial conditions as before is given as

$$\rho_{ee}(t) = \frac{\frac{1}{2}\Omega^2}{2\gamma^2 + \Omega^2} \left[1 - \left(\cos \lambda t + \frac{3\gamma}{2\lambda} \sin \lambda t \right) e^{-\frac{3\gamma t}{2}} \right], \quad (2.43)$$

with $\lambda = (\Omega^2 - 1/4\gamma^2)^{1/2}$.[21] This case will be the most relevant for experiments performed in Section 3.1, since the frequency of external field can easily be tuned to be resonant to the driven transition.

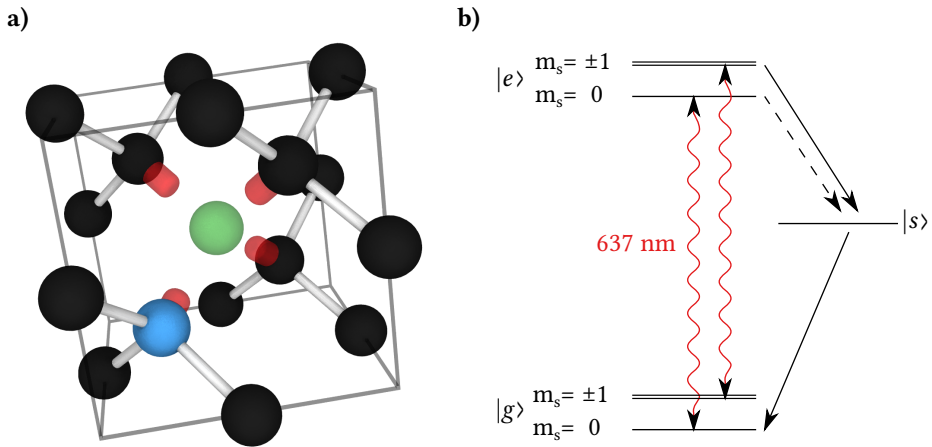


Figure 2.8: a) Structure of NV center in diamond and its close environment. The green sphere symbolizes the missing carbon atom next to the nitrogen atom (blue sphere). Red lobes represent dangling bonds. b) Simplified energy level scheme. Ground state and excited state are both triplet states. The metastable shelving state is singlet. Radiative transitions (curly red arrows) are mainly spin conserving between the excited and the ground state. Non-radiative transitions from the excited state to the shelving state preferably occur from the $|e, m_s = \pm 1\rangle$ states, and from there to the $|g, m_s = 0\rangle$ state.

2.2 Nitrogen vacancy centers in diamond

Diamond is a crystal consisting of carbon atoms in a face centered cubic (fcc) lattice with a two atom basis and a lattice constant of 3.56 Å.[23] With its wide band gap of 5.5 eV, it is optically transparent from the far infrared to the deep ultraviolet. [24] The extraordinary hardness (10 on the Mohs scale) and high refractive index of 2.4 are probably the features diamond is most commonly known for.[25]

Impurities in the diamond lattice can act as optically active color centers with the most prominent being the nitrogen vacancy center (NV center) shown in Figure 2.8. In an NV center, a carbon atom is replaced by a nitrogen atom and the lattice site next to the nitrogen is vacant. It therefore belongs to the C_{3v} symmetry group. It occurs in a neutral state (NV^0) and a negatively charged state (NV^-). The electronic structure of the negatively charged center involves six electrons of which three are provided by the dangling bonds from the surrounding carbon atoms, two from the nitrogen atom and one is captured from the lattice. In this thesis, only the NV^- center is examined and in the following simply referred to as NV center. Its additional electron gives rise to a spin structure for coherent manipulation.

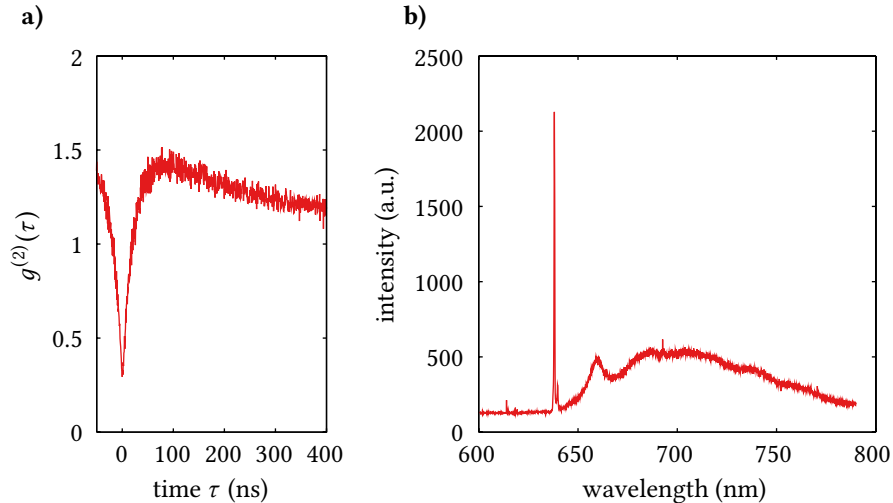


Figure 2.9: **a)** Typical second order autocorrelation function of the emmission of an NV center with bunching and antibunching behavior. **b)** Fluorescence spectrum of an NV center at 5.2 K. The zero phonon line (ZPL) at 637 nm and the phonon side band are clearly visible.

2.2.1 Optical properties

The optical properties of the NV center in diamond are remarkable. First of all, single NV centers are photostable single photon emitters, even at room temperature. This makes them a candidate for many potential applications that require single photon sources.[3] Figure 2.9 shows a typical measurement of the second order autocorrelation function $g^{(2)}$ of the optical emission of an NV center. As described in 2.1.1, a value close to zero at $\tau = 0$ clearly indicates the single photon emitter behavior.

Due to its symmetry, emission from the NV center occurs via two perpendicular dipoles. The basic photophysics of the NV center can be explained by the simplified energy level diagram shown in Figure 2.8. Similar to the one discussed in Section 2.1.1, it is a three level system consisting of a ground state $|g\rangle$ of symmetry 3A_2 , an excited state $|e\rangle$ of symmetry 3E and a metastable singlet state $|s\rangle$ with two levels of symmetries 1A_1 and 1E . The ground and excited states are further split into three spin sublevels with $m_s = -1, 0, 1$. This system will be sufficient to understand the experiments performed in Chapter 3, a more complete one derived from group theory is given in [26] and [6].

Shown in Figure 2.9 is a fluorescence emission spectrum of a single NV center at 5.2 K. The most prominent feature in the spectrum is the zero phonon line (ZPL) at 637 nm which corresponds to the transition from the excited state to the ground state when no phonons are involved. It accounts to roughly 5 % of the emission in contrast to the 95 % for which the vibrational phonon side band, that stretches from ca. 650 nm to 790 nm, is responsible. At room temperature, the phonon side band is even more pronounced and almost conceals the ZPL, making experiments that require single photons from the ZPL

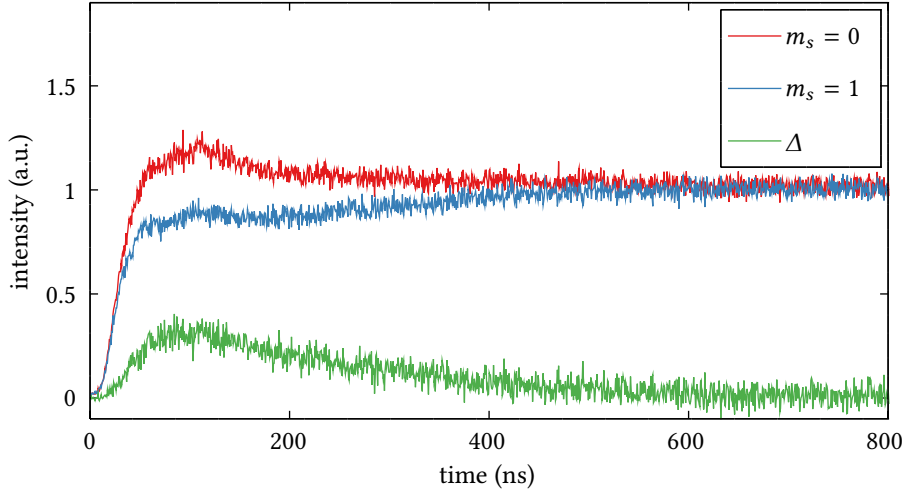


Figure 2.10: Temporal evolution of the fluorescence of the two spin states and their difference in fluorescence Δ . The $m_s = 1$ curve was measured by initializing the NV in the $m_s = 0$ state and flipping the spin with a π pulse. The red and blue curves were normalized with their fluorescence for times after 1500 ns before their difference (green curve) was calculated. After around 500 ns, the difference between the states vanishes and the NV center is in the equilibrium.

at room temperature rather impossible without structures like cavities, that selectively enhance the ZPL.[27] On the other hand, strong coupling to the phonon side band allows for off-resonant excitation of the NV center since spare energy of the excitation light can quickly dissipate into the phonon bath. In an experiment, excitation of the NV center with smaller wave lengths than the ZPL enables for convenient separation of the emission light via spectral filters.

2.2.2 Spin properties

As mentioned in the previous section, the electronic ground and excited states are triplet states with a zero field splitting of 2.87 GHz and 1.42 GHz respectively. Without an external field, for both triplets the two $m_s = \pm 1$ state energies are degenerated and the $m_s = 0$ state is energetically lower. The degeneracy can be lifted by applying a magnetic field, which causes the $m_s = \pm 1$ levels to shift in opposite directions due to the Zeemann effect. Optical transitions between states are spin preserving.

The metastable singlet state plays an important role for the NVs magneto-optical behavior. Due to different inter-system crossing rates for the spin states, the singlet manifold is mainly populated from the $|e, m_s = \pm 1\rangle$ states. Therefore, an electron in this state is more likely to decay via the singlet state, whereas an electron in the $|e, m_s = 0\rangle$ state preferably decays directly to the $|g, m_s = 0\rangle$ state via the radiative transition. A resulting optical contrast between both spin states of up to 30 % was observed in this

thesis. The $m_s = 0$ state is therefore often referred to as bright state, whereas the $m_s = \pm 1$ states are dark states. Additionally, deshelving from the metastable state happens predominantly to the $|g, m_s = 0\rangle$ state. As a result, after a few excitation cycles the NV center will most likely be initialized in the $m_s = 0$ state. Figure 2.10 shows the temporal evolution of the fluorescence intensities of the spin states.

2.2.3 Nano diamonds

If the size of a diamond is reduced to the order of nanometers, they are called nano diamonds. In the past, mainly used in industry for tasks like polishing that exploit their exceptional hardness, their optical and spin properties became a recent topic of research. Two main processes have emerged to produce nano diamonds on an industrial scale: synthesizing using high pressure and high temperature (HPHT) and harvesting from carbon detonations.[28] Other techniques like milling from bulk diamonds and bead assisted sonic disintegration (BASD) are used to produce nano diamonds on much smaller scales.[29] Depending on the production process, the purity and surface properties strongly differ as well as the amount and properties of eventually embedded defect centers. Additional defect centers can be implanted by ion beams.[30]

Spin properties like the coherence time T_2 of NV centers in nano diamond for instance are found to be inferior to the ones in bulk diamond and they are more prone to spectral diffusion of the ZPL.[31] Reasons for this can be strain in the diamond, the increased influence of the surface termination due to the smaller volume to surface ratio compared to bulk diamonds and charge traps and ionized impurities which lead to small fluctuations of the electric field environment and thereby stark shifts.[32, 33] The reported lifetimes of the excited state at room temperature is increased compared to bulk diamond (24 ns vs. 12 ns) attributed to their lower effective refractive index.[6] The main advantage of nano over bulk diamonds is their mobility and integrability into functional structure which is an important step for building future quantum hybrid systems.[8]

3 Experimentals

After the discussion of the theoretical fundamentals, the spin and optical properties of the NV center in nano diamond are investigated in the following two experiments.

First, the spin coherence of single NV centers in different types of nano diamonds will be investigated via spin manipulation experiments. Statistical measurements of their optically detected magnetic resonance (ODMR) contrast and their T_2 and T_2^* spin coherence times will be determined and give a benchmark of the nano diamonds performance.

In Section 3.2 the optical indistinguishability of two consecutively emitted photons from the same NV center is probed in a two photon quantum interference experiment.

3.1 Spin coherence of the NV center

3.1.1 Setup

In this section, the experimental setup for investigating spin coherence properties of the NV center that was developed during this thesis will be explained. The setup is based on the one built by Strauß et al.[34] Further emphasis was put on reliability and automatization. Therefore, tools and protocols were established to conveniently perform statistical measurements of many single NV centers. A simplified scheme of the setup is shown in Figure 3.1. Equipment only needed for technical reasons is not shown for reasons of clarity.

The experimental setup consists of a confocal scanning microscope, a microwave setup for spin manipulations and a Hanbury Brown and Twiss (HBT) interferometer to identify single emitters. The investigated nano diamonds are distributed on glass cover slips which are mounted on a manual xyz-stage using a sample holder. The sample holder incorporates a microwave antenna and a small magnet for spin manipulation experiments. The NV centers are excited by a green 532 nm continuous wave laser that is focused using an oil immersion objective lens with a high numerical aperture of $NA = 1.4$. Emitted fluorescence light is collected through the same objective lens and directed to the HBT setup. Alternatively, it is possible to direct emitted light to a spectrometer and a CCD camera by flipping mirrors. A bit pattern generator constantly loops the current experimental sequence which is around 5 μs long until it is reprogrammed to the next measurement step and thereby triggers the laser and microwave accordingly while the fluorescence signal is integrated for up to several seconds for each step. Therefore, each acquired data point is the result of thousands of cycles of one sequence. The individual parts are described as follows.

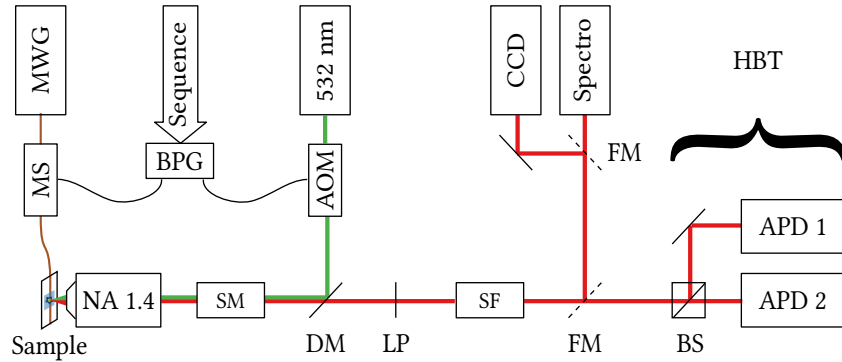


Figure 3.1: Schematics of the setup used for performing spin manipulation experiments. Abbreviations: MWG - microwave generator; BPG - bit pattern generator; AOM - acousto optical modulator; MS - microwave switch; CCD - CCD camera; Spectro - spectrometer; SM - scanning mirrors; SF - spacial filters; APD - avalanche photo diode; DM - dichroic mirror; LP - long pass filter; FM - flip mirror; BS - beam splitter; HBT - Hanbury Brown and Twiss interferometer.

Avalanche photo diodes and correlator

Two avalanche photo diodes (APDs) (Laser-Components Count-20C) in a Hanbury Brown and Twiss configuration were used to detect photons. Their specified dark count rate is below 20 counts/s and their quantum efficiency in the wave length range of the NV center emission is about 70 %. Furthermore, their dead time after registering a photon is typically 45 ns. Detected photons were correlated by connecting the APD output signals to the start and stop inputs of a TimeHarp 260 manufactured by PicoQuant. Also, fluorescence lifetime measurements were performed by adding the output signals and feeding the sum to the stop input while connecting the start input to the laser channel of the bit pattern generator. The maximum time resolution of the TimeHarp 260 is given as 25 ps and the dead time is less than 25 ns.

CCD camera

An ORCA-HR-C4742-85 Hamamatsu Digital Camera was used for quick imaging of the sample and to enable for easy adjustment of the focus and pinhole of the confocal microscope. Its thermoelectric cooled charge coupled device (CCD) chip has 10 million pixels and a minimum shutter speed of 330 μm .

Spectrometer

An Acton SpectraPro 500i 500 mm spectrometer with three gratings (600, 1200 and 1800 grooves/inch) mounted on a turret was used to take emission spectra of the investigated NV centers. The CCD chip of this spectrometer is cooled with liquid nitrogen to

about -90°C . The liquid nitrogen reservoir lasts for about twelve hours.

Laser source and Acousto Optical Modulator (AOM)

The laser source used for off-resonant excitation is a commonly used 532 nm continuous wave diode laser from Shanghai Laser Optics Century Ltd. The maximum output power was measured to be around 250 mW which translated to roughly 5 mW, measured directly in front of the microscope objective after the excitation beam has passed most of the setup including a single mode fibre for spacial filtering and the acousto optical modulator (AOM). The AOM (MT110-A1-VIs from AA opto-electronic) was used to switch on and off the laser accordingly to the desired pulse sequence. The switching time of the AOM is around 18 ns and the measured extinction ratio is around 2000:1. With this light source, it was easily possible to saturate the investigated NV centers. Additional optical attenuators and a continuously adjustable attenuator wheel in the excitation path were used to measure the saturation behavior of the NV center and to set the power accordingly. A photodiode, permanently incorporated into the excitation path via a 90:10 beam splitter, was used to conveniently measure the laser power.

Microwave setup

For the generation of the microwave radiation, an Agilent Technologies PSG analog signal generator was used. This generator is capable of generating cw signals with a power between -20 dBm and 12 dBm and is tunable in a frequency range from 250 kHz to 31.8 GHz. All settings of the generator can be controlled remotely via a LabView interface. A microwave switch manufactured by mini-circuits with a switching time around 2 ns chopped the microwave signal into pulses of a desired length. The resulting sequence was then amplified by a linear microwave amplifier and fed to the sample holder and the microwave antenna. For the first experiments, a simple gold wire was utilized as a near infrared antenna and pressed against a cover slip on which the nano diamonds were spin coated upon. Later, a wave guiding gold strip line was directly produced on the glass substrate via lithography and the diamonds were spin coated on top. Both techniques were found to give similar results concerning the manipulation of the NVs spin state. After passing the antenna, the microwave was converted into a power dependent voltage and read out by a digital oscilloscope.

Bit pattern generator

A bit pattern generator (USB-BITP-200) manufactured by DEDITEC was used to fastly trigger the AOM and the microwave switch according to the desired pulse sequence. The pulse sequence is conveniently programmable via USB and LabView. Once programmed, it is continuously looped until it is reprogrammed to a new sequence or the next time step by the software. The minimal temporal resolution of the bit pattern generator is 6.6 ns.

Digital oscilloscope

The digital outputs of the bit pattern generator, the microwave power signal and the signal of the photodiode were all fed into a fast digital oscilloscope (Tektronik MSO 2024B). This way, the current experimental sequence could be observed in real time which allowed for easy debugging and adjusting of the timings as well as compensating for electrical delays.

3.1.2 Sample and Preparation

The type of the investigated nano diamond and the preparation of the sample have a crucial influence on the outcome of the performed measurements. In the following, the used diamonds and preparation techniques are presented.

Nano diamonds

Three types of nano diamonds provided by Mircodiamant AG, Switzerland, are investigated in this thesis, they all have an average diameter of around 25 nm

1. Quantum Particle QP25 nano diamonds. The manufacturer performed different cleaning and annealing processes on the diamonds before shipping.
2. DiaScence 25 nano diamonds. They were also cleaned and annealed by the manufacturer, but were additionally irradiated with nitrogen atoms, to increase the amount of NV centers per diamond.
3. MSY mono-crystalline diamond powder, produced by HPHT synthesis. They were neither particularly cleaned nor annealed.

Cleaning and Spin-coating

In order to get a homogeneous distribution of the nano diamonds, they were spin-coated onto cover slips. Before spin-coating, the cover glasses were cleaned by rinsing them with acetone and isopropanol and then putting them into an ultrasonic bath in a surface functionalizing Hellmanex II solution for about 30 min. Cover slips with lithographed antennas were not put into the ultrasonic bath, since this would have destroyed the structure. The diamonds were diluted in ionized water to a concentration of around 2000:1. The diluted nano diamonds were also put into the bath for a couple of minutes to break diamond clusters. After blowing off left over liquids from the cover slips with nitrogen, 20 µL of the solution were spin-coated on the glasses by manually ramping the spin-coater speed to a maximum of around 2500 rounds/min while releasing the diamond droplets onto the center of the cover slip. The ramping was done in approximately 30 s and the total spin-coating time was set to 60 s.

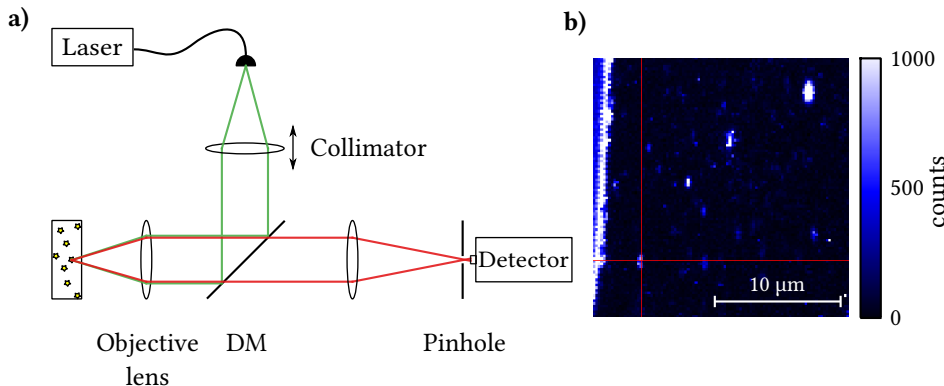


Figure 3.2: **a)** Working principle of a confocal microscope. **b)** Typical $20\text{ }\mu\text{m}$ by $20\text{ }\mu\text{m}$ 2D scan of a diamond sample, performed with a laser power of around $200\text{ }\mu\text{W}$ and an integration time of around 20 ms for each pixel. The red cross shows the current focus position locked on a nano diamond hosting a single NV center. The bright straight line at the left is the edge of the microwave antenna. Very bright and big spots like the one on the upper right are typically diamond clusters or other contaminations.

3.1.3 Methods

Scanning confocal microscopy

The working principle of confocal microscopy is illustrated in Figure 3.2. A confocal microscope uses point illumination and a pinhole in an optically conjugate plane in the detection path to eliminate signal that originates from the surroundings of the focused specimen. This effectively suppresses the collected background, enhancing the signal to noise ratio massively compared to a conventional wide field fluorescence microscope. Also, as only fluorescence light produced very close to the focus is detected, the images resolution, in particular in the sample depth direction, is increased. However, the point illumination requires scanning over the specimen to obtain 2D or 3D images. In the built setup, this is done by piezo-controlled xy-scanning mirrors and a z-piezo stage. The detection light is spatially separated from the excitation light by a dichroic mirror.

In order to compensate for eventual drifts of the observed NV centers position, a refocus routine was developed and implemented into the setup. After a certain time or when the fluorescence signal fell below an adjustable threshold, a small area around the current position of the laser focus was automatically scanned in all three dimensions and the focus was set to the position of maximum fluorescence again. This tracking algorithm enabled for long-term measurements on a single nano diamond over arbitrary time periods.

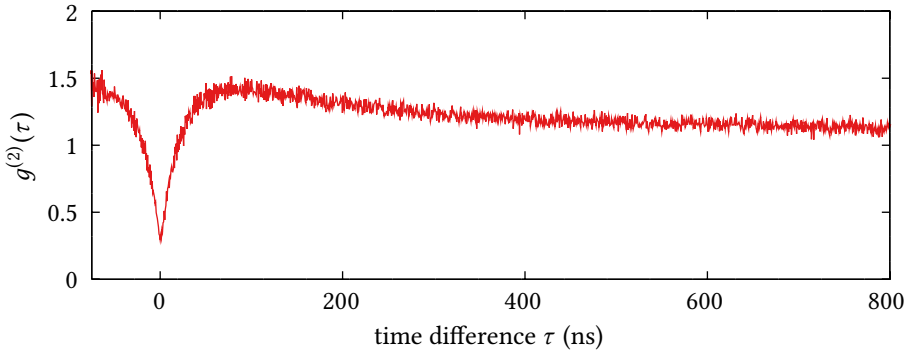


Figure 3.3: Typical bunching and antibunching behavior of the $g^{(2)}$ function of a single NV center measured with the Hanbury Brown and Twiss setup.

Hanbury Brown and Twiss setup

All emitters in the scanning plane, including undesired contaminations or nano diamonds that contain multiple NV centers, show up as bright spots on the microscope image. The Hanbury Brown and Twiss (HBT) setup can now be used to identify single NV centers by verifying their single photon emitter behavior discussed in Section 2.1.1. Such a HBT setup consists of a 50:50 beam splitter with two output ports, each connected to a single photon detector, i. e. an avalanche photo diode. A correlator starts a time measurement if one of the detectors registers a photon. A photon detected at the other detector stops the measurement. If the light originates from a single photon source, the detectors will never detect simultaneously one photon each. A HBT setup measures coincidences of photon detection events. In the limit of low count rates and short correlation times, the result of such a measurement is proportional to the $g^{(2)}$ function of the system. Even for single emitters, background fluorescence and the limited correlator resolution will prevent the autocorrelation function at zero time delay $g(0)^{(2)}$ from vanishing completely.

Optically Detected Magnetic Resonance (ODMR)

The spin-dependent luminescence of the NV center can be used to optically read out its spin state. In a typical ODMR experiment, the NV center is excited off-resonantly while an auxiliary microwave field is slowly swept over the resonances of the NVs level splitting between the $m_s = 0$ and the $m_s = \pm 1$ ground states. When the microwave field is resonant to the frequency that corresponds to the splitting, spin flops occur, resulting in a reduction of the fluorescence intensity. Figure 3.4.b shows the recorded fluorescence obtained while sweeping over the resonances. The degeneracy of the $m_s = \pm 1$ states was lifted by introducing a static magnetic field that shifted the resonances symmetrically around the zero field resonance at 2.87 GHz. A reference signal for normalization was measured for 200 μ s before the microwave was applied for another 200 μ s while reading out the spin state. The relatively long time gates ensured that most of the spin dynamics

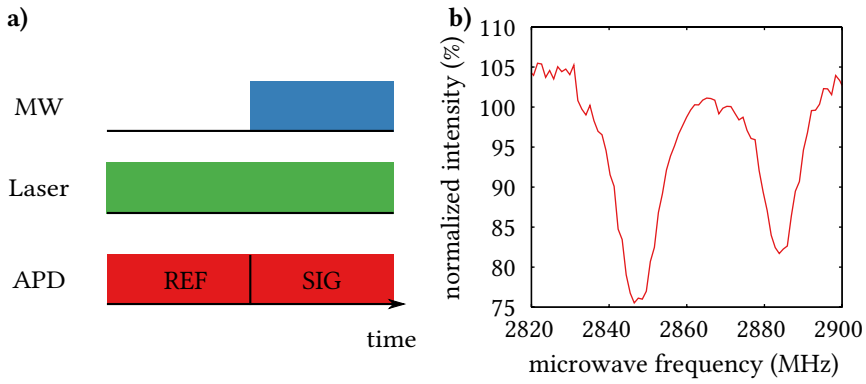


Figure 3.4: **a)** Measurement scheme and **b)** resulting signal of an ODMR measurement. The microwave intensity was set to 0 dBm at the microwave generator which was sufficient to saturate the intensity dip depths.

already abated and the measured signal mainly corresponded to the stable state solutions of the system discussed in Section 2.1.5. Every frequency step was typically integrated for one second while constantly looping the sequence to obtain an averaged fluorescence of the superposition state. A scheme of the measurement sequence is also shown in Figure 3.4.a.

Coherent spin manipulation

The most simple coherent spin manipulation experiment is to drive and detect Rabi oscillations. Therefore, the NV center is initialized in the $m_s = 0$ state by exciting it with the 532 nm cw laser source for 2 μ s. During the last microsecond, a reference fluorescence signal which is later used to normalize the actual spin dependent signal is recorded. Then, a microwave pulse resonant to the level splitting of the different spin states is applied for a time τ . Finally, the current spin state is read out by switching on the laser for 500 ns and measuring the fluorescence. Repeating this sequence continuously while stepwise increasing the duration of the microwave pulse τ results in the average fluorescence intensity of the spin state superposition in dependence of τ which oscillates according to the Rabi oscillations performed by the system. The measurement sequence and the resulting signal for a typical NV are shown in Figure 3.5. Since the NV center is initialized in the bright $m_s = 0$ state and due to the fact that the fluorescence signal will never completely vanish because of the limited contrast c between the states the intensity oscillations can be described by

$$I_{\text{Rabi}}(\tau) = S \cdot (1 - c \cdot \rho_{ee}(\tau)), \quad (3.1)$$

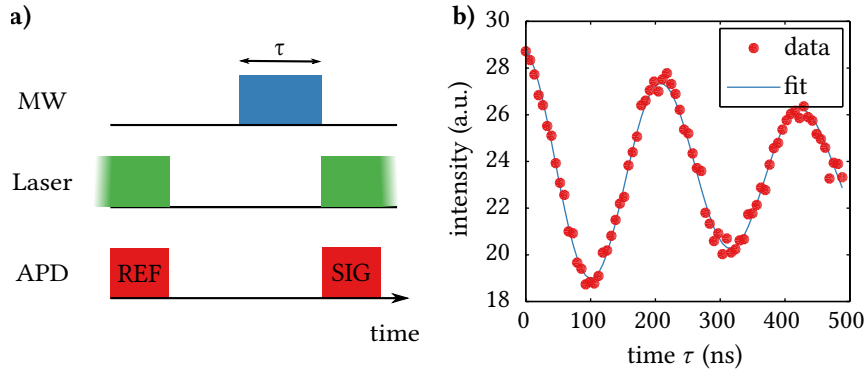


Figure 3.5: a) Measurement scheme of the Rabi sequence. The microwave intensity was set to 0 dBm at the microwave generator

where the scaling factor S is the relation between the integration times of signal and reference gate and signal gate. Using Equation 2.43, this results in:

$$I_{\text{Rabi}}(\tau) = S \cdot \left(1 - c \cdot \frac{\frac{1}{2}\Omega^2}{2\gamma^{*2} + \Omega^2} \left[1 - \left(\cos \lambda \tau + \frac{3\gamma^{*}}{2\lambda} \sin \lambda \tau \right) e^{-\frac{3\lambda\tau}{2}} \right] \right), \quad (3.2)$$

with $\lambda = (\Omega^2 - 1/4\gamma^{*2})^{1/2}$ and $\gamma^{*} = 1/T_2^{*}$. With this scheme, the Rabi frequency Ω , the decoherence time T_2^{*} and the Rabi contrast c can be determined.

When the microwave resonance frequency and the Rabi frequency of the NV are known, it is possible to perform the slightly more elaborate Hahn echo experiment. Here, after initializing in the $m_s = 0$ state, a $\pi/2$ pulse is applied to fully convert the populations into coherences. Now, the system is prone to dephasing. After a time τ , a π pulse is applied that inverts the coherence. Finally, after waiting for the time τ in which the static part of the dephasing refocusses again, a last $\pi/2$ pulse takes the system back to the $m_s = 0$ state and its fluorescence is read out. This sequence cancels the dephasing effect caused by static local field inhomogeneities and thereby enables the direct measurement of the T_2 time. According to theoretical calculations from Fanciulli et al., the Hahn echo decays as $e^{-(2\tau/T_2)^3}$. [35] Therefore, fitting the experimental data is done with the following formula:

$$I_{\text{Hahn}}(\tau) = A \cdot e^{-(2\tau/T_2)^3} + B. \quad (3.3)$$

A and B are fit parameters that are introduced to adapt the theory to the experimental conditions.

In general, the coherence properties of an NV center highly depend on the strength and direction of an external magnetic field.[26, 36] In the performed experiment, the magnetic field is provided by a magnet that is fixed on the sample holder. Its distance and the resulting field with respect to the investigated diamonds is therefore the same

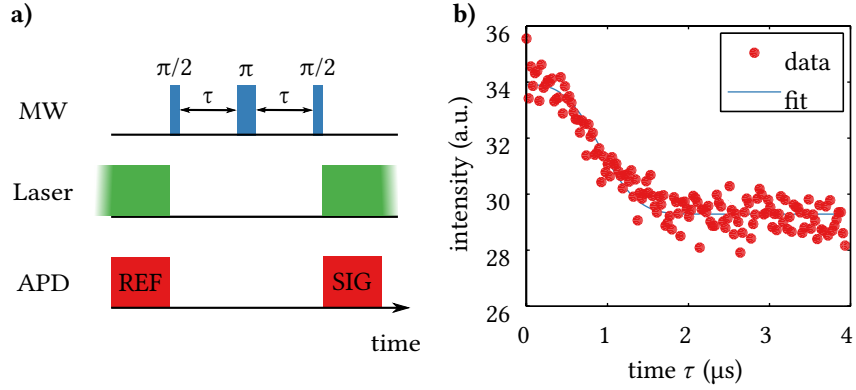


Figure 3.6: Measurement scheme and resulting signal of an Hahn echo experiment.

for all investigated samples. Nevertheless, the orientation of individual NV centers will be randomly distributed and as a result, the determined coherence times are expected to mirror that behavior. Other effects that have an influence on the spin coherence such as the concentration of carbon 13, and the surface termination of the diamond, will likely be the same for all diamonds in one batch.

3.1.4 Results

The obtained results are presented in this section. First, preliminary measurements were performed to determine the influence of laser and microwave power on the measured signal quality and spin physics and to develop strategies and protocols for measuring spin coherence times of many NV centers shown in Section 3.1.4.

Influence of the excitation laser power

In order to determine a suitable excitation power for NV centers and the described setup, saturation curves were recorded. As discussed in Section 2.1.3, for single photon emitters the saturation behavior of the detected fluorescence rate follows Equation 2.24.

Figure 3.7 shows a typical saturation curve. Each data point was integrated for one second. Fitting was done using Equation 2.24 with an assumed APD dark count rate of 40 counts/s and resulted in

$$\begin{aligned} R_{inf} &= (277 \pm 100) \text{ kcounts/s}, \\ P_{sat} &= (221 \pm 77) \mu\text{W}, \\ a_{bg} &= (74 \pm 112) \text{ kcounts}/\mu\text{W}, \end{aligned} \quad (3.4)$$

with a coefficient of determination $R^2 = 0.996$. The maximum signal to noise ratio was calculated to be 15.2 at a laser power of $11 \mu\text{W}$ and a total count rate of roughly 15 000 counts/s. Increasing the laser power to P_{sat} boosts the count rate by an order of

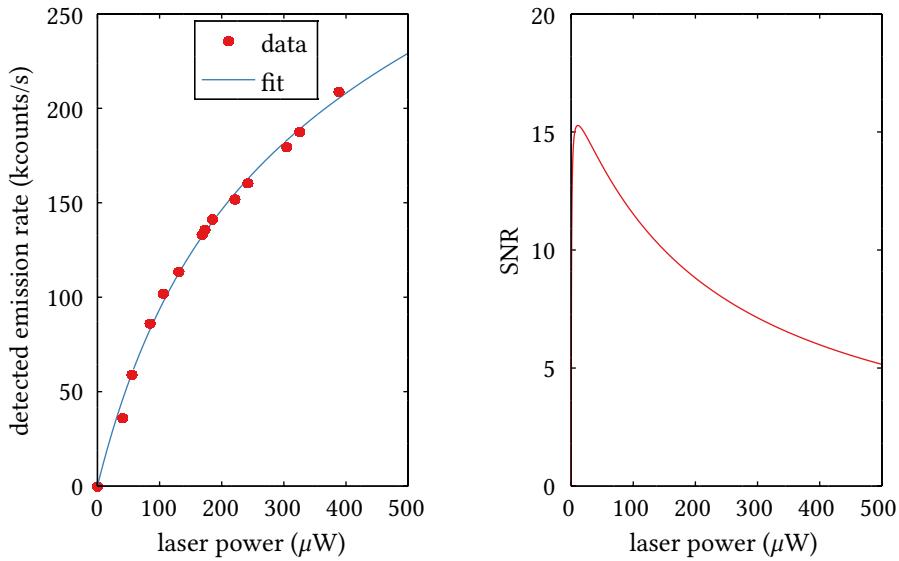


Figure 3.7: Measured saturation curve of a typical NV center and the behavior of the signal to noise ratio SNR calculated with the fit parameters found with Equation 2.24.

magnitude which allows for much faster data acquisition, but also worsens the signal to noise ratio to a value of around 8. Therefore, during the experiment, the excitation power was chosen to be above $11\text{ }\mu\text{W}$, to allow for convenient integration times at an acceptable signal to noise ratio. Of course, the saturation behavior for each individual NV can vary, i.e. because of the different local environment, but for the sake of comparability, the experiments performed in this section were performed with an excitation power of around $50\text{ }\mu\text{W}$.

Influence of the microwave power

After finding a good value for the laser power, the influence of the microwave power on the spin dependent optical contrast and the Rabi frequency was investigated. Figure 3.8 shows the evolution of the fluorescence signal difference between the two spin states and an ODMR scan for different microwave powers measured at the same NV center.

It becomes evident that the contrast improves with increasing microwave field intensities, but saturates for high field intensities. This is coherent with the results derived in Section 2.1.5 and illustrated in Figure 2.6. Also, the depolarization time in which the fluorescence difference between the two state vanishes is unaffected by a changed microwave power and stays at around 500 ns. Nevertheless, two main processes limit the power used for spin manipulations in the experiment. First, at high microwave powers the electric resistance of the thin gold wire or the strip line caused it to heat up and

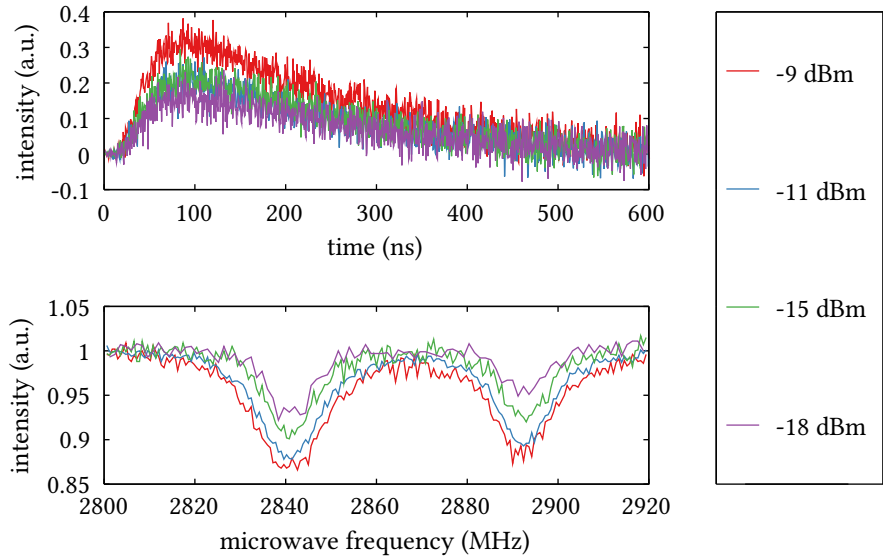


Figure 3.8: Top: Evolution of the difference in the fluorescence signals for different microwave powers. Bottom: ODMR scans of another NV at different excitation powers. The $m_s = +1$ and $m_s = -1$ levels were split by applying weak static magnetic field.

expand. This introduced movements of the wire or could even cause a burning through of the strip line. Second, as seen in Figure 3.8 an increased microwave power causes a broadening of the resonance dips. This phenomenon is the power broadening discussed in Section 2.1.5. Therefore, for the following measurements, power was kept as low as possible but as high as needed to get into the contrast saturation regime. Values of 6 dBm set at the microwave generator before amplification were never exceeded to preserve the antenna from heat damage.

With this in mind, Rabi oscillations between the spin states of one NV center were measured at different microwave powers. As stated in Section 2.1.5, the Rabi frequency Ω is given by

$$\Omega = \frac{\mathbf{d} \cdot \mathbf{E}_0}{\hbar}, \quad (3.5)$$

where \mathbf{d} is the dipole matrix element of the transition and E_0 is the amplitude of the oscillating field. The scalar product between the two entities yields a strong dependence on the angle and distance between the microwave antenna and the orientation of the NV embedded in the randomly disturbed nano diamond. This results in varying Rabi frequencies at the same microwave powers for different NVs and also, as seen in Figure 3.8, in different ODMR resonance dip depths corresponding to the orthogonal dipole matrix elements of the $m_s = \pm 1$ states that are split by a static magnetic field.

For a single NV center, the Rabi frequency can be tuned by varying the power of

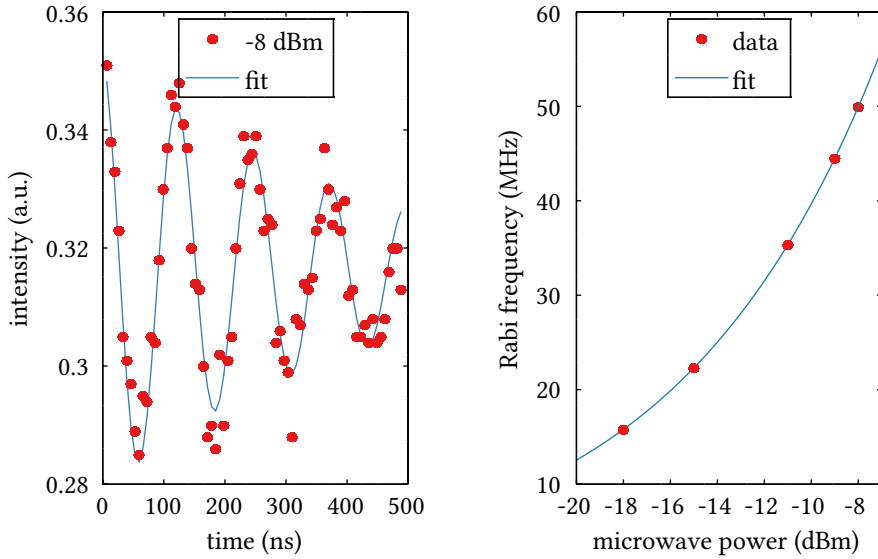


Figure 3.9: Rabi oscillations and their microwave power dependence for one NV center. Each oscillation was fit with Equation 3.2 and the resulting Rabi frequencies are plotted on the right. The power dependency is fit with Equation 3.7 which results in a proportionality constant $a = 125.5 \pm 0.8$ and a coefficient of determination of $R^2 = 0.999$.

the applied microwave. From Equation 3.5 follows a proportionality between the Rabi frequency and the microwave field amplitude. This translates into a proportionality between the Rabi frequency and the square root of the microwave power in Watts. The relation between Decibel-milliwatts, the unit of power that is mainly used in this thesis and also set at the microwave generator, and Watts is

$$P[W] = 1 \text{ mW} \cdot 10^{P[\text{dBm}] / 10}. \quad (3.6)$$

The dependence of the Rabi frequency on the microwave power in Decibel-milliwatts therefore becomes

$$\Omega(P) = a \sqrt{10^{P[\text{dBm}] / 10}}, \quad (3.7)$$

with the proportionality constant a . This constant is specific for every NV and its position as well as orientation with respect to the microwave antenna. Figure 3.9 shows a recorded oscillation at a microwave power of -9 dBm and the dependence of the Rabi frequency when the power is varied.

Statistical measurements of the ODMR contrast and the T_2^* and T_2 spin coherence times

After investigating the influence of the laser and microwave power and developing strategies to find optimal values for both of these parameters, it was possible to conveniently

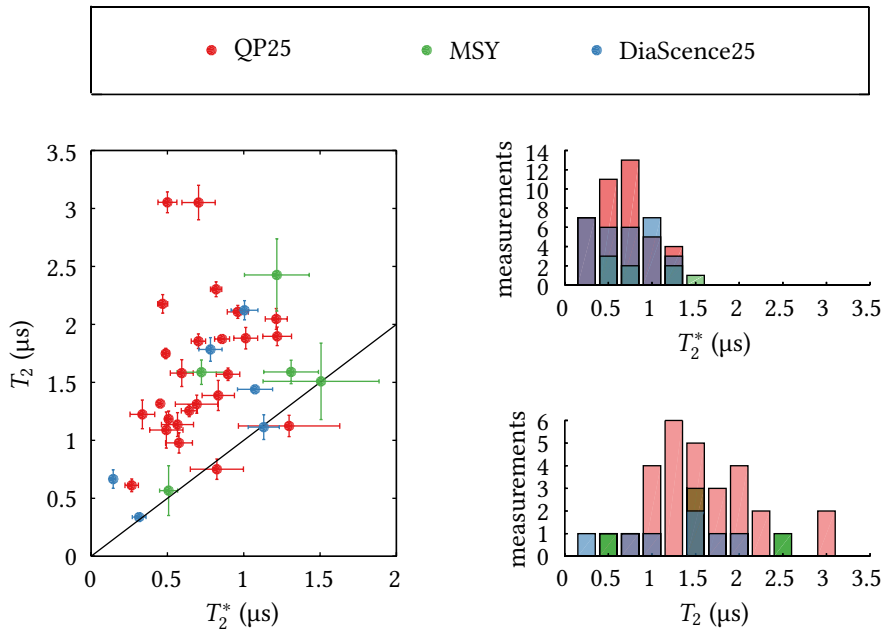


Figure 3.10: Obtained values of the T_2^* and T_2 spin coherence times for the different types of nano diamond. The black line in left graphs represents the case of no dephasing $T_2 = T_2^*$. The different color bars are drawn with transparency so that the colors mix when they overlap.

perform many measurements of the relaxation times for many NV centers in different types of nano diamonds.

The protocol for measurements was to first perform an xy-scan of the sample with the confocal microscope. After a potential NV was found and focused, the HBT setup was used to confirm the single photon source behavior with the typical bunching and anti-bunching behavior of a negatively charged NV center. In the next step, the resonance frequencies of the $m_s = 0 \leftrightarrow m_s = \pm 1$ transitions were determined in an ODMR measurement. A magnet that was fixed on the sample holder provided a small static magnetic field that lifted the degeneracy of the $m_s = \pm 1$ states. Then, Rabi oscillations were driven at both of the resulting resonances to determine the Rabi frequency and the T_2^* time. After that, the resulting Rabi frequencies were used to calculate the lengths of the π and $\pi/2$ pulses necessary for the Hahn echo sequence. With this sequence the T_2 time for each resonance was finally determined and the next NV center could be investigated.

In order to efficiently perform statistics of the T_2 and T_2^* times of multiple NVs, the measurement steps that involved coherent spin manipulation sequences, namely ODMR scanning, driving of Rabi oscillations and the Hahn echo experiment, were automated

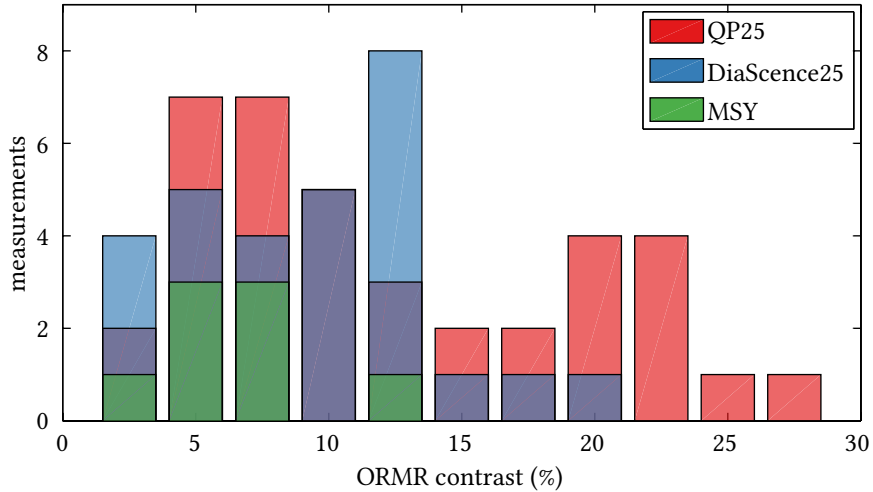


Figure 3.11: Achieved ODMR contrasts for different diamond types. The different color bars are drawn with transparency so that the colors mix when they overlap.

using LabView. After each step, it was automatically decided if it either should be repeated in order to enhance the signal quality by further integrating and averaging or if the current result is sufficient to go on with the next step. This decision was made by fitting with the corresponding equation and checking if the obtained uncertainties of the fit parameters were in a set allowed range. With this method, it was possible to measure the spin dynamics of a single NV center within roughly one hour. Figure 3.10 finally shows the obtained values for the T_2^* and T_2 spin coherence times for the different types of nano diamond. It can be noted, that within the uncertainties the inequality $T_2 > T_2^*$ holds for every investigated NV center. The weighted mean averages and its standard errors are summarized in Table 3.1.

The success of the protocol varied strongly for the different types of nano diamonds. The QP25 diamonds performed best. Almost every investigated diamond showed a strong bunching and anti bunching of the $g^{(2)}$ function, indicating the NV centers single emitter behavior. The recorded ODMR scans showed an average contrast of $(12 \pm 1)\%$ with single values up to 30 %. The results of the DiaScience25 diamonds were little worse with an average contrast of $(8 \pm 1)\%$. Also, approximately only every 10th fluorescing diamond carried a single NV center and was further investigated, which made gathering data for many NV centers very time consuming. The MSY diamonds performed worst, their average contrast was $(7 \pm 3)\%$ and it was very hard to find diamonds with single NV centers. This is reflected in the amount of obtained data shown in Figure 3.11 and Figure 3.10.

diamond type	T_2^* (μ s)	T_2 (μ s)	ODMR contrast (%)
QP25	0.56 ± 0.05	1.6 ± 0.1	12 ± 1
DiaScence25	0.53 ± 0.06	1.1 ± 0.3	8 ± 1
MSY	0.7 ± 0.1	1.5 ± 0.3	7 ± 3
all types	0.63 ± 0.05	1.6 ± 0.1	10 ± 1

Table 3.1: Weighted mean values and standard errors of the T_2^* and T_2 spin coherence times and the ODMR contrast of shown in Figure 3.10 and Figure 3.8.

3.2 Two photon quantum interference with a single NV center

Recent experiments showed that the ZPL of the NV center in nano diamond is subject to spectral diffusion.[31] Those experiments claim a time in the order of $5\text{ }\mu\text{s}$ in which two consecutively emitted photons have the same wave length. Here, it is tried to prove that within this time range, photons emitted from an NV center are indistinguishable. This is achieved by a two photon quantum interference experiment with photons originating from the same NV center.

3.2.1 Setup

For investigating the optical stability of NV centers ZPL, the setup in Section 3.1 was extended by a cryostat and a fiber-coupled beam splitter. Also, the excitation light source was changed to a tunable pulsed supercontinuum laser. The investigated nano diamonds were spin-coated on the back of a hemispherical solid immersion lens to maximize the collected emission. Emission of the ZPL is spatially separated from the phonon side band which is used for confocal scanning and emitter tracking by an 10 nm wide band filter. To superimpose two emitted photons at the fibre 50:50 beam splitter, they are directed along two optical paths of different length. The paths are realized by using an additional polarization-maintaining fibre as a delay line for one of the paths. The repetition rate of the laser was set to 17.1 MHz which exactly matches the travel time difference of the photons in the two paths. A polarizing beam splitter and a $\lambda/2$ plate were used to equally distribute the linear polarized light of the NV centers two perpendicular dipoles to the polarization maintaining fibres. With a probability of 25% , two successively emitted photons therefore impinge on the fiber-coupled beam splitter simultaneously. The mutual polarization of the two paths was adjusted using another $\lambda/2$ plate. A very crucial aspect of the setup is the maximization of the total counts collected from the zero phonon line and the long term stability of the setup that is needed for integrating over long periods of time. Maximum count rates of 2000 counts/s and integration times of up to 40 h on single NV centers, could be achieved.

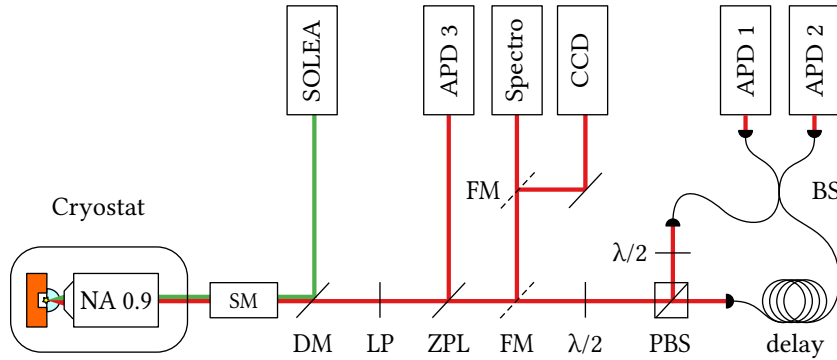


Figure 3.12: Schematics of the setup used for the Hong-Ou-Mandel type experiment, Abbreviations: CCD - CCD camera; Spectro - spectrometer; SM - scanning mirrors; SF - spacial filters; APD - avalanche photo diode; DM - dichroic mirror; LP - long pass filter; ZPL - zero phonon line filter; FM - flip mirror; PBS - polarizing beam splitter; BS - fiber beam splitter.

Laser source

A pulsed supercontinuum laser (SOLEA) provided by PicoQuant was used to periodically excite the NV centers. It is capable of generating pulses of less than 230 ps. Built-in spectral filters can be used to select a tunable wavelengths with a bandwidth down to 3 nm (FWHM) in a spectral range from 480 nm to 700 nm. The maximum average output power after the wavelength selector is around 1 mW for each 5 nm of bandwidth at a repetition rate of 40 MHz. The repetition rate can be set to fixed values between 2.5 MHz to 40 MHz of a built-in internal oscillators or triggered externally to a desired value in that range by a frequency generator, as done in this experiment.

Low temperature setup

To achieve the low temperatures needed to suppress the NV centers phonon side band and maximize the emission within the ZPL, a continuous flow cold finger cryostat (Type Microscope, Cryovac) was used. It was operated with liquid Helium, mainly at temperatures of around 5 K. At this temperature, a 100 L liquid Helium dewar lasted for about 48 h. Generally, even lower temperatures down to 4.3 K were achievable, but came at the cost of an exorbitantly increased Helium consumption. During operation, a vacuum with a pressure below 1×10^{-6} mbar inside the sample chamber was established to thermally isolate the sample from the environment. Inside the chamber, an objective lens manufactured by Mitutoyo with an NA of 0.9 and a working distance of 1.4 mm was installed to efficiently collect light.

In the past, long term fluorescence measurements of samples inside the cryostat were nearly impossible, because over time fluorescing contaminations accumulated in the laser focus and slowly outshined the actual measurement signal more and more.

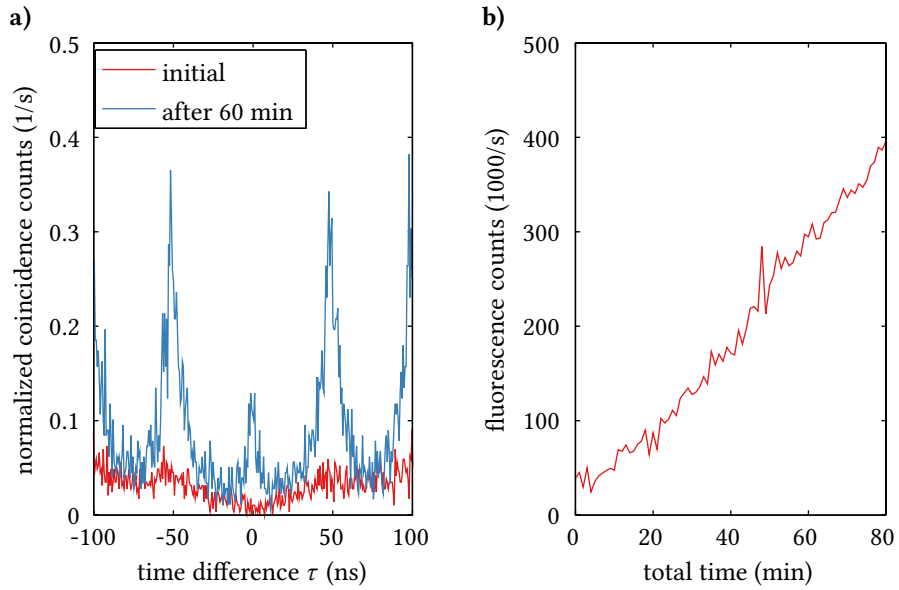


Figure 3.13: **a)** Correlation measurements of the same single NV center normalized directly after finding and focusing the NV center and after 60 min. For better comparability, both curves are normalized by their integration time of about 2 min. The mean excitation power of the pulsed laser was set to $50 \mu\text{W}$ measured directly before the cryostat at a repetition rate of 20 MHz. **b)** Time evolution of the total detected fluorescence during the same measurement. The fluorescence roughly tenfolds, significantly worsening the signal to noise ratio and concealing the single photon behavior.

The exact origin of these contaminations remains unclear. At normal pressure and room temperature, contaminations can often be oxidized and bleached to a level where they do not affect the measurement by applying a strong laser. Since samples in the isolation vacuum of the cryostat showed the exact opposite behaviour it can be assumed, that without the surrounding air these contaminations can not be oxidized anymore. Additionally, already present contaminations in the cryostat might sublime in the residual vacuum and then be trapped in the laser focus by tweezer effects. Extensive cleaning of all the parts that are exposed to the vacuum improved this behavior only partially. Reducing the excitation laser power slowed-down the contamination process, but the resulted in lower count that rates made longer integration times necessary and also the tracking of the NV center more difficult.

What finally solved the problem was to completely separate the investigated diamonds from the cryostat's vacuum by using a special sample holder design which is shown in below.

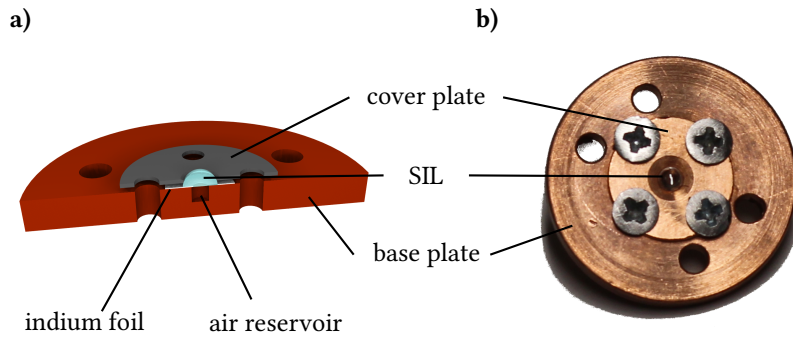


Figure 3.14: a) Rendered image of a cut through the middle of the sample holder and the SIL. b) actual picture of the assembled sample holder. The diamonds on the flat side of the SIL are completely isolated from the environment.

Solid immersion lens

To increase the amount of collected light, the nano diamonds were distributed on the flat back side of a semi-spherical Zirconiumdioxide ZrO_2 solid immersion lens (SIL) with a diameter of 2 mm. The SILs were purchased from a commercial vendor (Mikop, Switzerland). The higher refractive index of $n = 2.17$ at a wavelength of $\lambda = 600 \text{ nm}$ and the resulting higher density of optical states in relation to the surrounding air causes NV centers in close proximity to the surface to preferably emit light into the direction of the SIL and also decreases internal reflection on the diamond- ZrO_2 interface.[37, 38]

Sample holder

In order to isolate the diamonds from the environment and possible contaminations the sample holder shown in Figure 3.14 was designed. The SIL with the diamonds on the flat side is pressed onto the copper base plate by the stainless steel cover plate. A hole, in the center of the base plate, with the radius of 0.5 mm and a depth of 1 mm, serves as a small air reservoir that can be cleaned and controlled much more effectively than the whole cryostat. A ring of indium foil with a central hole is aligned between the SIL and the baseplate and effectively seals the space below the SIL.

3.2.2 Sample and Preparation

Nano diamonds

The diamonds used here are the already known QP25 provided by Microdiamant AG which performed best in the previous experiment.

Cleaning and spin-coating

The cleaning and spin-coating procedure was essentially the same as in the previous experiment. The sample holder was cleaned in the ultrasonic bath just like the cover slips before in Section 3.1.2. Since the ZrO_2 surface of the SIL is hydrophobic, the concentration of the diamond solution had to be increased to 1:750 in order to get a sufficient distribution of diamonds on the surface. In general, the results of the spin-coating on the SIL turned out to be less predictable than on glass cover slips which was mainly due the small size of the SIL that further complicated the process.

3.2.3 Methods

Two photon quantum interference

The unnormalized $G^{(2)}$ function of two photons, both produced by a two level system, that interfere on a beam splitter with the transmission and reflection coefficients T and R is given by

$$G^{(2)}(\tau, \delta\tau) = T^2 \exp\left(-\frac{|\tau|}{T_1}\right) + R^2 \exp\left(-\frac{|\tau - 2\delta\tau|}{T_1}\right) - 2RT \exp\left(-\frac{|\tau|}{2T_1} - \frac{|\tau - 2\delta\tau|}{2T_1} + \frac{|\tau - \delta\tau|}{T_1} - \frac{2|\tau - \delta\tau|}{T_2^*}\right), \quad (3.8)$$

where τ is the detection time difference and $\delta\tau$ is the time delay of the photons due to differences in their path lengths.[39] The excited state life time T_1 and the optical coherence time T_2^* are again the characteristic times known from the optical two level system. It can be noted that the coherence time T_2^* corresponds to the reciprocal line width of the emission spectrum of the two level system. In the performed experiment, the transmission and reflection coefficients of the fiber beam splitter were $T = R = 0.5$ and the repetition rate of the pulsed laser was adjusted in order to superimpose two condescending emitted photons that take different paths after the polarizing beam splitter, with zero time delay $\delta\tau = 0$ at the fiber-coupled beam splitter Equation 3.8 therefore yields

$$G^{(2)}(\tau) = \frac{1}{2} \exp\left(-\frac{|\tau|}{T_1}\right) - \frac{1}{2} \exp\left(-\frac{2|\tau|}{T_2^*}\right). \quad (3.9)$$

It becomes evident that in the ideal case of no dephasing $T_2^* = T_2 = 2T_1$, the $G^{(2)}$ function vanishes completely and in the case of $T_2^* \rightarrow 0$, there will be no two photon interference visible.

In the experiment, a single NV center serves as a photon source. It emits photons via its two perpendicular dipoles which are typically not degenerate. This will decrease the measured decoherence time T_2^* since it effectively broadens the line width of the emission spectrum. Nevertheless, a signature of the two photon quantum interference should be observable, since even for short coherence times the $G^{(2)}$ function reaches zero at $\tau = 0$.

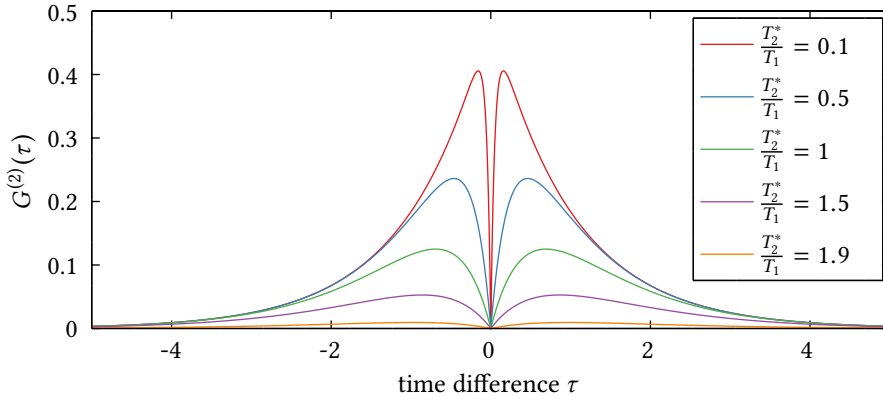


Figure 3.15: Shape of the unnormalized $G^{(2)}$ function given in Equation 3.9 for different ratios of $\frac{T_2^*}{T_1}$.

3.2.4 Results

Although the improved sample holder allows for long-term measurements at cryogenic temperatures, the achieved count rate collected from the ZPL is still crucial for the success of this experiment. Despite all the effort and the highly efficient collection optics, a sufficient value was not achieved in the experiment. As a last resort, the repetition rate of the exciting laser was therefore doubled to a value of 34.2 MHz and the averaged laser excitation power was set to $70 \mu\text{W}$. The wavelength of the laser was set to 570 nm as suggested by Wolters et. al in order to minimize spectral diffusion rate of the ZPL.[31] With this settings, a maximum count rate of about 2000 counts/s measured with both APDs was achieved.

A coincidence measurement of the full emission spectrum, including the phonon side band of the investigated NV center is shown in Figure 3.16. The measurement was performed with the free space setup from the previous experiment which could still be operated by simply changing the beam path with flip mirrors. Without the need to couple the emitted light into fibers, a total count rate of about 70 kcounts/s was measured.

Figure 3.17 finally shows the obtained signal that was gathered in a total time of around 20 h. The measurement was performed in intervals of 15 min. Every second interval was a reference measurement for which the polarization of the short arm was rotated by 90° . This resulted in an accumulated integration time of 10 h for each configuration. The time resolution of the correlator was 1.616 ns/channel. The shape of the relevant central peak shows a small deviation compared to the reference which is due to the Hong-Ou-Mandl effect.

To fit the data, two peaks before and after the one at $\tau = 0$ had to be taken into account, since the doubled repetition rate caused those peaks to potentially reach into the central one. Assuming an infinite time resolution, this range of the recorded signal can be described for the reference and the actual two photon quantum interference

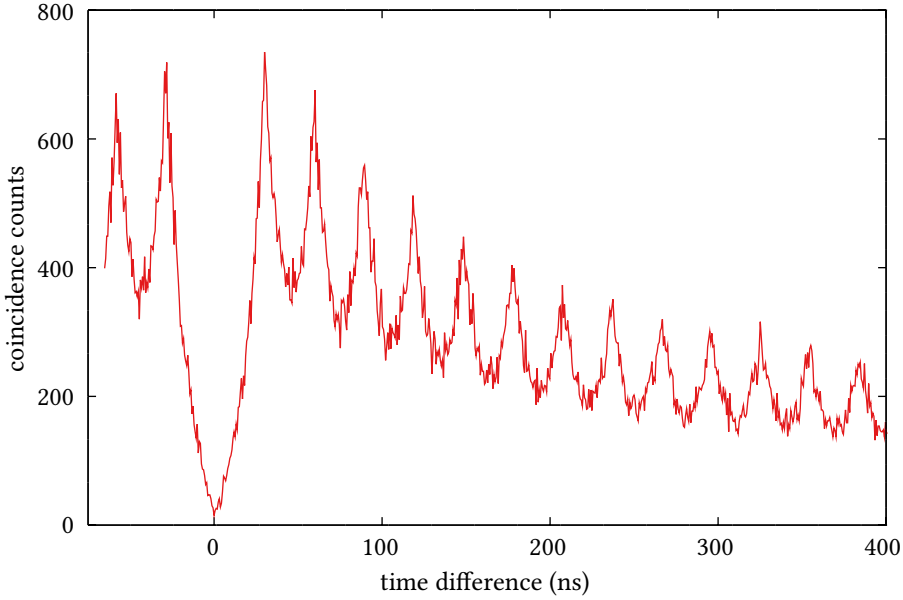


Figure 3.16: Coincidence measurement of the full emission spectrum of the investigated single NV center, recorded with the free space setup at an averaged excitation power of $70\text{ }\mu\text{W}$. The doubled repetition rate of 34.2 MHz of the excitation laser causes the detected pulses to overlap. The typical antibunching behavior of a single photon emitter is still very visible.

measurement as

$$N_{TPQI}(\tau) = -N_0 \exp\left(-\frac{2|\tau|}{T_2^*}\right) + \sum_{i=2}^2 N_i \exp\left(-\frac{|i \cdot \Delta + \tau|}{T_1}\right),$$

$$N_{Ref}(\tau) = \sum_{i=2}^2 N_i \exp\left(-\frac{|i \cdot \Delta + \tau|}{T_1}\right), \quad (3.10)$$

where $\Delta = 30.9\text{ ns}$ is the time between two pulses and N_i is the height of the measured pulse. It can further be assumed that the function is symmetric around $\tau = 0$ and therefore $N_i = N_{-i}$.

The finite resolution is considered by convolving Equation 3.10 with the response function of the correlator which is a Gaussian function with the width of the correlator resolution. This was done numerically in the fitting process. The results for the central feature of both configurations are given in Table 3.2.

An obtained coherence time of $T_2^* = (1 \pm 2)\text{ ns}$ would correspond to the spectral width of around 1 GHz . But the high uncertainties and the low coefficients of determination for the obtained values clearly show that higher count rates and longer integration times are necessary to reliably draw conclusions from the experiment.

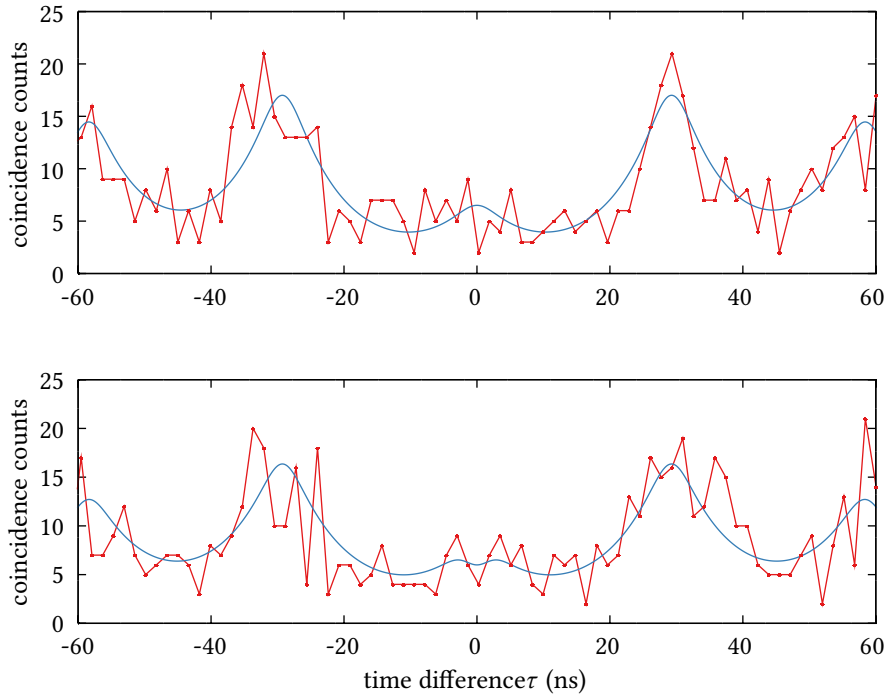


Figure 3.17: Result of the coincidence measurements for the reference configuration (upper graph) and the two photon quantum interference configuration (lower graph). The different shapes of the central features are a first signature of the Hong-Ou-Mandel effect.

	N_0 (a.u.)	T_1 (ns)	T_2^* (ns)	R^2
Reference	12 ± 3	8.2 ± 0.6	-	0.64
TPQI	15 ± 5	9 ± 1	1 ± 2	0.48

Table 3.2: Results of fitting the experimental data with the convolution of Equation 3.10 and a Gaussian function of the width of the time resolution.

4 Conclusion and outlook

During the course of this work, basic spin manipulation experiments such as Rabi oscillations and Hahn echos were successfully implemented and further elaborated for first statistical measurements of different kinds of nano diamonds. Now, the performance of different types of diamonds can easily be compared by the same standards. This is the first step in systematically searching for ways to improve the properties of the embedded NV centers. Many tools have been developed in this context like the software for confocal scanning and emitter tracking as well as the holder for the solid immersion lens which are all universally usable for many different kinds of nano emitters in the future.

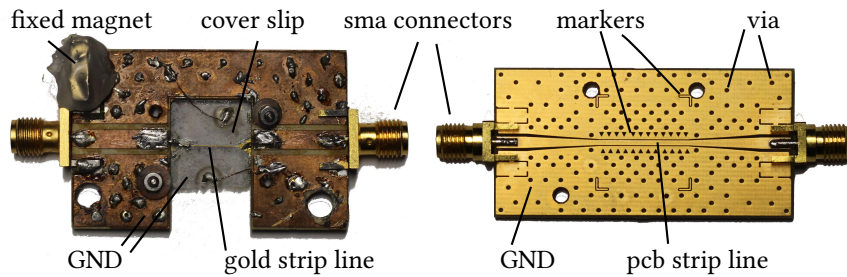


Figure 4.1: Left: Sample holder and microwave antenna design used during this thesis. The lithographed strip line antenna was destroyed during the annealing process of the nano diamonds. Right: New sample holder design with integrated antenna.

Concerning the performed spin coherence experiment, instead of statistical measurements of the spin properties, mapping NVs and measuring their performance before and after applying surface changing processes like annealing would give more precise information on the direct influence of surface properties on a specific NV center. In fact, during the experiment some investigated nano diamonds were already located and mapped while using the lithographed strip line antenna. But the annealing process destroyed the antenna structure and made further analysis impossible. For future experiments, a different sample holder design with the microwave antenna fabricated directly as an element of the printed circuit board has already been designed and is shown in Figure 4.1 right next to the destroyed lithographed antenna version. With the help of markers and latches, the cover slip with the nano diamonds can be placed very precisely on the sample holder. With this new configuration the nano diamonds on the glass can be investigated and mapped, then separated from the holder and processed via annealing before they are finally placed back into their original position where they can be found

again for further investigations.

Regarding the two photon interference experiment, even though it was possible to overcome major technical challenges, namely the occurring fluorescence problem in the cryogenic environment, the low count rates obtained from the ZPL still make the experiment very cumbersome. For repeating the Hong-Ou-Mandel type experiment, increasing the collection efficiency or maximizing the ZPL-emission is a major priority. This could be achieved by using selectively enhancing structures. For example, a Bragg mirror grown on top of the nano diamonds on the flat side of the SIL which reflects light at the wavelength of the ZPL could potentially double the collected emission.

Bibliography

- [1] *Standards 22 nanometers technology backgrounder*. Santa Clara, CA: Intel Corporation, 2011.
- [2] P. Shor. “Polynomial-Time Algorithms for Prime Factorization and Discrete Logarithms on a Quantum Computer.” In: *SIAM Rev.* 41.2 (Jan. 1, 1999), pp. 303–332. ISSN: 0036-1445. DOI: 10.1137/S0036144598347011. URL: <http://pubs.siam.org/doi/abs/10.1137/S0036144598347011> (visited on 11/10/2014).
- [3] T. D. Ladd et al. “Quantum computers.” In: 464.7285 (Mar. 4, 2010), pp. 45–53. ISSN: 0028-0836, 1476-4687. DOI: 10.1038/nature08812. URL: <http://www.nature.com/doifinder/10.1038/nature08812> (visited on 10/15/2013).
- [4] J. Wrachtrup and F. Jelezko. “Processing quantum information in diamond.” In: *J. Phys.: Condens. Matter* 18.21 (May 31, 2006), S807. ISSN: 0953-8984. DOI: 10.1088/0953-8984/18/21/S08. URL: <http://iopscience.iop.org/0953-8984/18/21/S08> (visited on 11/10/2014).
- [5] J. Cai et al. “A large-scale quantum simulator on a diamond surface at room temperature.” In: *Nat Phys* 9.3 (2013), pp. 168–173. ISSN: 1745-2473. DOI: 10.1038/nphys2519. URL: <http://www.nature.com/nphys/journal/v9/n3/full/nphys2519.html> (visited on 11/10/2014).
- [6] M. W. Doherty et al. “The nitrogen-vacancy colour centre in diamond.” In: 528.1 (July 2013), pp. 1–45. ISSN: 03701573. DOI: 10.1016/j.physrep.2013.02.001. URL: <http://linkinghub.elsevier.com/retrieve/pii/S0370157313000562> (visited on 10/13/2014).
- [7] A. Gruber et al. “Scanning Confocal Optical Microscopy and Magnetic Resonance on Single Defect Centers.” In: *Science* 276.5321 (June 27, 1997), pp. 2012–2014. ISSN: 0036-8075, 1095-9203. DOI: 10.1126/science.276.5321.2012. URL: <http://www.sciencemag.org/content/276/5321/2012> (visited on 11/10/2014).
- [8] J. Wolters. “Quantum hybrid systems.” PhD thesis. Berlin: Humboldt-Universität zu Berlin, Mathematisch-Naturwissenschaftliche Fakultät I, Oct. 8, 2013.
- [9] H. Bernien et al. “Heralded entanglement between solid-state qubits separated by three metres.” In: *Nature* 497.7447 (2013), pp. 86–90. ISSN: 0028-0836. DOI: 10.1038/nature12016. URL: <http://www.nature.com/nature/journal/v497/n7447/full/nature12016.html> (visited on 10/23/2014).
- [10] G. de Lange et al. “Single-Spin Magnetometry with Multipulse Sensing Sequences.” In: *Phys. Rev. Lett.* 106.8 (Feb. 24, 2011), p. 080802. DOI: 10.1103/PhysRevLett.106.080802. URL: <http://link.aps.org/doi/10.1103/PhysRevLett.106.080802> (visited on 11/10/2014).

- [11] F. Dolde et al. “Electric-field sensing using single diamond spins.” In: *Nat Phys* 7.6 (June 2011), pp. 459–463. ISSN: 1745-2473. doi: 10.1038/nphys1969. URL: <http://www.nature.com/nphys/journal/v7/n6/full/nphys1969.html> (visited on 11/10/2014).
- [12] A. W. Schell et al. “Scanning Single Quantum Emitter Fluorescence Lifetime Imaging: Quantitative Analysis of the Local Density of Photonic States.” In: *Nano Lett.* 14.5 (2014), pp. 2623–2627. ISSN: 1530-6984. doi: 10.1021/nl500460c. URL: <http://dx.doi.org/10.1021/nl500460c> (visited on 11/10/2014).
- [13] R. Schirhagl et al. “Nitrogen-Vacancy Centers in Diamond: Nanoscale Sensors for Physics and Biology.” In: 65.1 (Apr. 2014), pp. 83–105. ISSN: 0066-426X, 1545-1593. doi: 10.1146/annurev-physchem-040513-103659. URL: <http://www.annualreviews.org/doi/abs/10.1146/annurev-physchem-040513-103659> (visited on 09/18/2014).
- [14] R. J. Glauber. “Quantum theory of optical coherence: selected papers and lectures.” In: 130.6 (1963). doi: 10.1103/PhysRev.130.2529. URL: <http://link.aps.org/doi/10.1103/PhysRev.130.2529>.
- [15] C. K. Hong, Z. Y. Ou, and L. Mandel. “Measurement of subpicosecond time intervals between two photons by interference.” In: *Phys. Rev. Lett.* 59.18 (Nov. 2, 1987), pp. 2044–2046. doi: 10.1103/PhysRevLett.59.2044. URL: <http://link.aps.org/doi/10.1103/PhysRevLett.59.2044> (visited on 11/06/2014).
- [16] J. L. O’Brien, A. Furusawa, and J. Vučković. “Photonic quantum technologies.” In: 3.12 (Dec. 2009), pp. 687–695. ISSN: 1749-4885, 1749-4893. doi: 10.1038/nphoton.2009.229. URL: <http://www.nature.com/doifinder/10.1038/nphoton.2009.229> (visited on 10/15/2013).
- [17] T. Legero et al. “Characterization of single photons using two-photon interference.” In: (Dec. 2, 2005). arXiv: quant-ph/0512023. URL: <http://arxiv.org/abs/quant-ph/0512023> (visited on 10/20/2014).
- [18] S. Schietinger. “Investigation, manipulation, and coupling of single nanoscopic and quantum emitters.” PhD thesis. Humboldt-Universität zu Berlin, Mathematisch-Naturwissenschaftliche Fakultät I, 2012. URL: <http://edoc.hu-berlin.de/dissertationen/schietinger-stefan-2012-03-01/METADATA/abstract.php?id=39768> (visited on 10/02/2014).
- [19] F. Jelezko and J. Wrachtrup. “Single defect centres in diamond: A review.” In: 203.13 (Oct. 2006), pp. 3207–3225. ISSN: 18626300, 18626319. doi: 10.1002/pssa.200671403. URL: <http://doi.wiley.com/10.1002/pssa.200671403> (visited on 10/01/2014).
- [20] H. J. Metcalf. *Laser cooling and trapping*. In collab. with P. Van der Straten. Graduate texts in contemporary physics. New York: Springer, 1999. 323 pp. ISBN: 0387987479.
- [21] R. Loudon. *The quantum theory of light*. 3rd ed. Oxford science publications. Oxford ; New York: Oxford University Press, 2000. 438 pp. ISBN: 0198501773.

- [22] F. Bloch. “Nuclear Induction.” In: 70.7 (Oct. 1946), pp. 460–474. ISSN: 0031-899X, 1536-6065. doi: 10.1103/PhysRev.70.460. URL: <http://link.aps.org/doi/10.1103/PhysRev.70.460> (visited on 10/05/2014).
- [23] H. Ibach and H. Lüth. *Festkörperphysik Einführung In Die Grundlagen*. Springer DE, 2009. (Visited on 06/30/2013).
- [24] M. Fox. *Optical properties of solids*. Oxford [etc.]: Oxford University Press, 2001. ISBN: 0198506120.
- [25] C. Kittel. *Introduction to solid state physics*. 8th ed. Hoboken, NJ: Wiley, 2005. 680 pp. ISBN: 047141526X.
- [26] J. R. Maze et al. “Properties of nitrogen-vacancy centers in diamond: the group theoretic approach.” In: 13.2 (Feb. 28, 2011), p. 025025. ISSN: 1367-2630. doi: 10.1088/1367-2630/13/2/025025. URL: <http://stacks.iop.org/1367-2630/13/i=2/a=025025?key=crossref.8ab36e601bb08ebf4241a2745f14eb4d> (visited on 10/08/2014).
- [27] Q. Liu, Z. Ouyang, and S. Albin. “Photonic crystal nano-cavities for enhancing zero-phonon line emission from nitrogen-vacancy centers in diamond.” In: *Optics & Laser Technology* 48 (June 2013), pp. 128–134. ISSN: 0030-3992. doi: 10.1016/j.optlastec.2012.09.033. URL: <http://www.sciencedirect.com/science/article/pii/S0030399212004628> (visited on 11/10/2014).
- [28] A. Krueger. “Beyond the shine: recent progress in applications of nanodiamond.” In: 21.34 (2011), p. 12571. ISSN: 0959-9428, 1364-5501. doi: 10.1039/c1jm11674f. URL: <http://xlink.rsc.org/?DOI=c1jm11674f> (visited on 10/12/2014).
- [29] E. Neu et al. “Narrowband fluorescent nanodiamonds produced from chemical vapor deposition films.” In: 98.24 (2011), p. 243107. ISSN: 00036951. doi: 10.1063/1.3599608. URL: <http://scitation.aip.org/content/aip/journal/apl/98/24/10.1063/1.3599608> (visited on 10/12/2014).
- [30] I. Aharonovich et al. “Chromium single-photon emitters in diamond fabricated by ion implantation.” In: 81.12 (Mar. 2010). ISSN: 1098-0121, 1550-235X. doi: 10.1103/PhysRevB.81.121201. URL: <http://link.aps.org/doi/10.1103/PhysRevB.81.121201> (visited on 10/13/2014).
- [31] J. Wolters et al. “Measurement of the Ultrafast Spectral Diffusion of the Optical Transition of Nitrogen Vacancy Centers in Nano-Size Diamond Using Correlation Interferometry.” In: 110.2 (Jan. 9, 2013). ISSN: 0031-9007, 1079-7114. doi: 10.1103/PhysRevLett.110.027401. URL: <http://link.aps.org/doi/10.1103/PhysRevLett.110.027401> (visited on 10/13/2014).
- [32] A. Majumdar, E. D. Kim, and J. Vučković. “Effect of photogenerated carriers on the spectral diffusion of a quantum dot coupled to a photonic crystal cavity.” In: 84.19 (Nov. 2011). ISSN: 1098-0121, 1550-235X. doi: 10.1103/PhysRevB.84.195304. URL: <http://link.aps.org/doi/10.1103/PhysRevB.84.195304> (visited on 10/13/2014).

- [33] P. Tamarat et al. “Stark Shift Control of Single Optical Centers in Diamond.” In: 97.8 (Aug. 2006). ISSN: 0031-9007, 1079-7114. doi: 10.1103/PhysRevLett.97.083002. URL: <http://link.aps.org/doi/10.1103/PhysRevLett.97.083002> (visited on 10/13/2014).
- [34] M. Strauß. *Kohärente Spinmanipulation am Stickstofffehlstellenzentrum in Diamant*. Berlin: Humboldt-Universität zu Berlin, Oct. 31, 2013.
- [35] M. Fanciulli, ed. *Electron Spin Resonance and Related Phenomena in Low-Dimensional Structures*. Red. by C. E. Ascheron and A. H. Duhm. Vol. 115. Topics in Applied Physics. Berlin, Heidelberg: Springer Berlin Heidelberg, 2009. ISBN: 978-3-540-79364-9, 978-3-540-79365-6. URL: <http://link.springer.com/10.1007/978-3-540-79365-6> (visited on 10/17/2014).
- [36] P. L. Stanwix et al. “Coherence of nitrogen-vacancy electronic spin ensembles in diamond.” In: *Phys. Rev. B* 82.20 (Nov. 17, 2010), p. 201201. doi: 10.1103/PhysRevB.82.201201. URL: <http://link.aps.org/doi/10.1103/PhysRevB.82.201201> (visited on 11/12/2014).
- [37] A. Schell. “Photonic Applications and Hybrid Integration of Single Nitrogen Vacancy Centres in Nanodiamond.” PhD thesis. Berlin, Sept. 31, 2014.
- [38] T. Schröder. “Integrated photonic systems for single photon generation and quantum applications.” PhD thesis. Berlin: Humboldt-Universität zu Berlin, Mathematisch-Naturwissenschaftliche Fakultät I, 2013. URL: <http://edoc.hu-berlin.de/dissertationen/schroeder-tim-2012-08-30/METADATA/abstract.php?id=40056> (visited on 11/10/2014).
- [39] J. Bylander, I. Robert-Philip, and I. Abram. “Interference and correlation of two independent photons.” In: *Eur. Phys. J. D* 22.2 (Feb. 1, 2003), pp. 295–301. ISSN: 1434-6060, 1434-6079. doi: 10.1140/epjd/e2002-00236-6. URL: <http://link.springer.com/article/10.1140/epjd/e2002-00236-6> (visited on 10/29/2014).

List of publications

Poster

Bernd Sontheimer, Niko Nikolay, Max Strauß, Andreas W. Schell, Janik Wolters, and Oliver Benson, "Coherence Properties of Nitrogen Vacancy Centers in Nano Diamond", DPG Frühjahrstagung Dresden, Session MA 48.6, April 2014

Selbstständigkeitserklärung

Hiermit erkläre ich, dass ich die vorliegende Arbeit selbstständig und nur unter Zuhilfenahme der angegebenen Quellen und Hilfsmittel verfasst habe.

Berlin, December 2, 2014

Bernd Sontheimer